Chinese Chemical Letters 36 (2025) 109906

Contents lists available at ScienceDirect

Chinese Chemical Letters

journal homepage: www.elsevier.com/locate/cclet

Iridium-based catalysts for oxygen evolution reaction in proton exchange membrane water electrolysis

Jiawei Ge[a,b], Xian Wang[b], Heyuan Tian[b], Hao Wan[b], Wei Ma[c], Jiangying Qu[a,*], Junjie Ge[b,*]

[a] Dongguan Key Laboratory of Low-Carbon Recycling and Utilization, School of Environment and Civil Engineering, Dongguan University of Technology, Dongguan 523808, China
[b] School of Chemistry and Materials Science, University of Science & Technology of China, Hefei 230026, China
[c] State Grid Anhui Electric Power Research Institute, Hefei 230601, China

ARTICLE INFO

Article history:
Received 21 January 2024
Revised 24 March 2024
Accepted 17 April 2024
Available online 18 April 2024

Keywords:
Iridium-based catalysts
Oxygen evolution reaction
Proton exchange membrane water electrolysis
Degradation mechanism
Optimized strategies
Practical application

ABSTRACT

Proton exchange membrane water electrolysis (PEMWE) is a favorable technology for producing high-purity hydrogen under high current density using intermittent renewable energy. The performance of PEMWE is largely determined by the oxygen evolution reaction (OER), a sluggish four-electron reaction with a high reaction barrier. Nowadays, iridium (Ir)-based catalysts are the catalysts of choice for OER due to their excellent activity and durability in acidic solution. However, its high price and unsatisfactory electrochemical performance severely restrict the PEMWE's practical application. In this review, we initiate by introducing the current OER reaction mechanisms, namely adsorbate evolution mechanism and lattice oxygen mechanism, with degradation mechanisms discussed. Optimized strategies in the preparation of advanced Ir-based catalysts are further introduced, with merits and potential problems also discussed. The parameters that determine the performance of PEMWE are then introduced, with unsolved issues and related outlooks summarized in the end.

© 2025 Published by Elsevier B.V. on behalf of Chinese Chemical Society and Institute of Materia Medica, Chinese Academy of Medical Sciences.

1. Introduction

The increasing demand for green and sustainable energy calls for the search for green energy carriers [1–4], *i.e.*, exploiting renewable energy resources like wind, solar, and hydropower [5]. These resources, however, suffer from a huge limit due to intermittent availability in time- and space-insurmountable disadvantages that make it difficult to meet specific usage scenarios [6,7]. Hydrogen molecules, with high energy density and clean nature, are one of the most promising energy carriers. H_2 generation is currently produced almost entirely through steam reforming using fossil fuels [8], accompanied by the usage of 6% global natural gas and 2% global coal [7]. In contrast, water electrolysis that converts water into H_2 could produce green H_2 at a large scale and high purity [9]. Water splitting coupling renewable energy also offsets the intermittent limit of these energy resources in time and space with great promise [5,10].

Water electrolysis is made up of two half-cell reactions, the hydrogen evolution reaction (HER) at the cathode and the oxygen evolution reaction (OER) at the anode [8,11,12]. The HER that involves the transfer of two electrons and the formation of simple intermediates is relatively easy to occur. The OER, however, a four-electron transfer process with multiple intermediates, poses a great limit in reaction kinetics and energy efficiency of the whole water splitting process [13,14]. It thus requires a higher voltage than the theoretical limit of 1.23 V *vs.* RHE to proceed with OER. The electrocatalysts can play a key role in accelerating the transition of intermediates and reducing the overpotentials (η) of OER electrocatalysts [15–17].

The pH of electrolytes poses a great effect on the reaction pathways of OER, which determines the reaction rate of the whole water splitting [18–22]. In alkaline electrolytes, free hydroxyl groups (OH^-) are adsorbed, oxidized, and converted into H_2O and O_2 [18]. In acid solutions, the initial break of the covalent O–H bond of H_2O needs to proceed for oxidizing H_2O and generating O_2, which consumes extra energy to trigger the following reaction [22,23]. Despite favorable reaction kinetics for alkaline electrolytes, acidic OER based on proton-exchange membrane water electrolysis (PEMWE) technology, also presents some crucial characteristics, compatible with highly fluctuating energy (a rapid response in 10 s) [8,18]. Compared with other ion membranes, modern PEMWE, consisting of perfluorinated sulphonic acid copolymer membranes, delivers a much smaller gas crossover, promising for a low gas mixture of H_2/O_2 (99.999 vol% H_2) for safe operation [7,13,24].

* Corresponding authors.
E-mail addresses: qujianggaofeng@163.com (J. Qu), gejunjie@ustc.edu.cn (J. Ge).

https://doi.org/10.1016/j.cclet.2024.109906
1001-8417/© 2025 Published by Elsevier B.V. on behalf of Chinese Chemical Society and Institute of Materia Medica, Chinese Academy of Medical Sciences.

Furthermore, such a sandwich structure of anode, proton-conducting polymer electrolyte, and cathode, namely membrane-electrode assembly (MEA), promotes proton transfer, thereby leading to low ohmic resistivity and high current density (operated over 2 A/cm^2) [8,25]. Moreover, a compact energy storage and conversion system can be designed *via* coupling PEMWE cells and PEM fuel cells (PEMFCs) [7,8]. Given water disassociation and adsorption restrained by H_2/O_2 gas bubbles, externally applied fields, such as gravity [26], centrifugal acceleration field [27], and a magnetic field [28], can be used to assist gas bubble desorption. Besides, the properties of catalyst layers are essential to favor water disassociation and adsorption. The introduced Mo at IrMo intermetallic can form stable-adsorbed OH intermediates due to a thermodynamically favorable water dissociation process [29], which is beneficial to the following reaction routes. These favorable features above attract much attention to PEMWE for green hydrogen production.

However, some fatal factors, especially strong acids and a high oxidation environment, pose a big restriction on electrocatalyst selection in PEMWE [16,30]. Typically, Ir-based catalysts appear as one of the most favorable alternatives used in OER due to their high anticorrosion merits, excellent catalysis activity and high electronic conductivity [15,31,32]. However, the low abundance in earth and the high cost of Ir restrict it from commercialization. Nowadays, it is thus essential to explore low-loading Ir catalysts with high catalysis activity and stability for reducing the price used in OER [33,34]. Two fundamental features, namely active site density and intrinsic activity, have aroused wide attention to increasing the usage of Ir as much as possible [35]. For example, some strategies from composition optimization [29,36,37] to structure and morphology modification [38–40] are adopted to improve the catalytic activity and durability in acid solution. As a matter of fact, the understanding of Ir-based catalysts is still not enough to elucidate the catalytic mechanism of Ir-based electrocatalysts, and thus the mechanism-guided exploitation of low-Ir electrocatalysts is still lack.

In this review, we summarize the recent progress of Ir-based electrocatalysts for acid OER to shed light on its catalytic mechanism and structural design. First, the reaction mechanisms for acid OER are analyzed to determine the key effect of Ir sites on OER with high activity and stability. We then discuss some key descriptors to evaluate the stability and activity of Ir-based OER catalysts. Following that, some typical strategies along with their mechanism are highlighted for designing advanced catalysts as well as intrinsic structure-performance relationships. Apart from some great efforts in Ir-based OER catalysts, advanced characterization methods are commented to comprehend their catalytic mechanism conveniently. Finally, the challenges and perspectives of Ir-based OER catalysts are under debate to shed insight into advanced low-Ir catalysis for acid OER.

2. Catalytic mechanism under acid condition

The four-electron transfer of OER at anode poses a great overpotential on electrocatalysts, which demand a higher potential to initiate such a four-electron transfer. Meanwhile, such a high potential causes the overoxidation of electrocatalysts and further element dissolution. These complex processes and factors on a four-electron transfer and high potential impose much uncertainty on their catalytic mechanism. Therefore, the exploration of high activity and stability of electrocatalysts under acid conditions is pivotal to promote oxygen production efficiency [41–43]. Nowadays, it is generally accepted pathways for OER in acid solution are adsorbate evolution reaction (AEM), lattice oxygen mechanism (LOM), and novel oxide path mechanism (OPM) [16,30,44,45]. However, the basic principles of electrochemical water decomposition are still blurry, which do not meet the basic request for the rational design of electrocatalysts with high activity and stability.

2.1. Reaction routes

2.1.1. Adsorbate evolution mechanism (AEM)

The well-accepted AEM reveals that the generated oxygen molecules derive from adsorbed water molecules on the catalyst's surface, including three oxygen-containing intermediates, OH*, O* and OOH* (Fig. 1a). First, one water molecule attacks the active site, and two successive deprotonation processes occur to produce OH* and O*, respectively. And then, another water molecule is absorbed on the O* site coupling the removal of H^+ from the second water molecule to form *OOH*. Finally, accompanied by the last deprotonation process and its desorption, O_2 is created from active sites, and meanwhile, active sites reverse back to the initial states [24,31,46].

$$H_2O^* \rightarrow OH^* + H^+ + e^- \quad (1)$$

$$OH^* \rightarrow O^* + H^+ + e^- \quad (2)$$

$$O^* + H_2O \rightarrow OOH^* + H^+ + e^- \quad (3)$$

$$OOH^* \rightarrow O_2 + H^+ + e^- \quad (4)$$

Theoretically, the minimum overpotential, which is generally considered as 0 V, is governed by the largest difference between the free energy difference of neighbor elementary steps [23,47]. Of note, the transformation of oxygen-containing intermediates poses impressive energy barriers, delivering the overpotential with a larger value. The universal scaling relationship of OH* and OOH* is used to describe the binding energy of reaction intermediates ($\Delta G_{OOH} = \Delta G_{OH} + 3.2$ V) [48,49]. As a rule of thumb, the binding energies of reaction intermediates are neither too strong nor too weak according to Sabatier's theory [23]. The strong binding energy of oxygen-containing intermediates leads to the difficulty in forming OOH*, suppressing the whole oxygen-generated processes; on the contrary, the weak binding energies restrict the transformation of OH* to O* [50,51]. Therefore, the optimal binding energies located on the volcano-top sites need to be modulated for the minimum overpotential of 370 mV [36,52]. However, to date, much work claims that an overpotential lower than 370 mV is obtained, meaning that a popular mechanism plays a vital role in bypassing the theoretical overpotential limit of AEM theory on OER.

2.1.2. Lattice oxygen mechanism (LOM)

On the contrary of AEM along with stable surface sites for oxygen evolution processes, LOM route bypasses the formation of the reaction intermediate of OOH*, breaking the overpotential limit from the scaling relationship of ΔG_{OOH} and ΔG_{OH}. LOM is triggered by the activation of lattice oxygen (O_L) on its surface [51,53,54]. The initial two elementary steps of LOM are the same as that of AEM, namely two successive deprotonation processes for forming reaction intermediates of OH* and O* (Fig. 1b). Next, the activated O_L is coupled with O* to produce an O_2 molecule after the desorption of O–O species on the active site. Afterward, the vacancy (O_V) left by O_L is attacked and refilled by another water molecule [55]. Accompanied by the removal of the proton of this water molecule, active sites are returned for the following cycles [56–58].

$$H_2O^* \rightarrow OH^* + H^+ + e^- \quad (5)$$

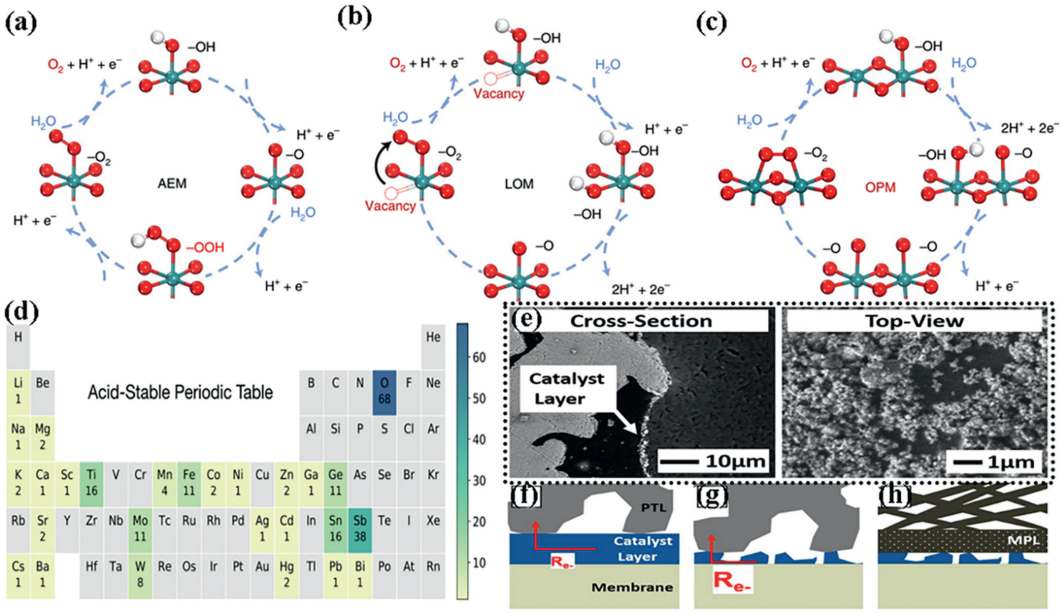

Fig. 1. Schematics of OER mechanisms. Schematic illustration of simplified OER mechanisms. (a) The AEM. (b) The LOM. (c) The OPM. Reproduced with permission [67]. Copyright 2021, Springer Nature. (d) Frequency at which each element appears in acid-stable oxides. Elements with zero frequency are shaded in gray. Lanthanoids and actinoids are omitted for clarity because no oxide containing these elements was predicted to be stable. Reproduced with permission [95]. Copyright 2020, American Chemical Society. (e) SEM images with cross section and top view (0.2 mg_{Ir}/cm^2_{MEA}), (f) homogeneous catalyst layer (>1 mg_{Ir}/cm^2_{MEA}), (g) a thin, inhomogeneous catalyst layer (<0.5 mg_{Ir}/cm^2_{MEA}), (h) the replacement of Ti porous transport layer by microporous carbon layer. Reproduced with permission [97]. Copyright 2018, The Author(s).

$$OH^* \rightarrow O^* + H^+ + e^- \quad (6)$$

$$O^* + O_L \rightarrow O_2 + O_V \quad (7)$$

$$O_V + H_2O \rightarrow O_L + H^* + H^+ + e^- \quad (8)$$

$$H^* \rightarrow * + H^+ + e^- \quad (9)$$

Though lattice oxygen participating in oxygen evolution reaction effectively reduces the transformation barriers of oxygen-containing intermediates, the relatively high O 2p band energy, corresponding to high-LOM-triggered activation states [30,59], imposes structural instability. In general, the d band of metal is located on the top of the O 2p band, and continuous oxidation of cations leads to the decline of Fermi level until aligning with O_2/H_2O redox potential, which initiates the O_L-participating OER. Usually, increasing M-O bond covalency and oxygen vacancy density enables to modulate Fermi levels lower than that of O_2/H_2O redox potential [60–63], beneficial to water oxidation. Such a process can result in the easy escape of lattice oxygen and metal species from catalyzers, namely structural instability. For an ideal catalyzer utilized in OER, a trade-off between activity and stability needs to be balanced *via* customizing AEM and LOM.

2.1.3. Oxide path mechanism (OPM)

Ideally, direct O–O coupling without the participation of lattice oxygen can maintain high activity and structural stability under OER at the same time [64–66]. Intensive researches announce the breakthrough of their overpotential uninvolving lattice oxygen. One pathway of skipping the formation of OOH*, namely OPM, is proposed to elucidate the evolution of oxygen-containing intermediates for heterogeneous catalysis (Fig. 1c). Similar to AEM and LOM, first, one water molecular attacks active sites with the removal of proton to form OH* and O*. Meanwhile, another similar reaction occurs on the neighbor active sites for forming O*. Finally, two neighbor O* moieties are directly coupled into O–O species, and accompanied by the release of O–O species, O_2 molecules are obtained.

OPM skips the formation of OOH*, delivering relatively low reaction barriers lower than 370 mV for breaking the theoretical limit of the scaling relationship [67]. Compared with AEM (single active site), it is necessary to elaborately modify the distance of two neighbor active sites for direct coupling of O* species. The interatomic M-M distance is too big to trigger the direct coupling of two neighbor O* moieties under OPM theory [68]. Thus, the grand challenge of OPM is the geometric configuration of active sites for benefiting the direct coupling of O* moieties.

2.2. The dissolution issue for Ir-based catalysts

2.2.1. The challenge in detecting and analyzing its dissolution mechanisms

Activity and stability of Ir-based catalysts for OER are the major concerns for practical application, which keep a reverse relationship intuitively. Intensive efforts are developed to oxidation-state changes of catalysts, including Ir catalysts, which are considered as the driving force of oxygen evolution processes [69]. The increase in applied potentials on Ir catalysts leads to charge storage on active sites [70], which further induces the adsorption of oxygen-containing intermediates on active sites [71,72]. Therefore, on the initial states, applied potentials on the anode cause the increase of oxidation of Ir sites. Since its complex intermediates along with four-electron transfer may become unstable under service conditions, Ir catalysts suffer from the element dissolution and thereby performance degradation. Nowadays, it is generally accepted that the participation of Ir^{III} species and the formation of volatile Ir^{VI} species are two main Ir dissolution routes under operation [56,57,73,74].

The grand challenge in determining the Ir dissolution mechanism is to probe the transformation of interfacial intermediates during OER. To date, S-numbers [75,76] are accepted as unifying experiment parameters to measure the dissolution rate of metal as

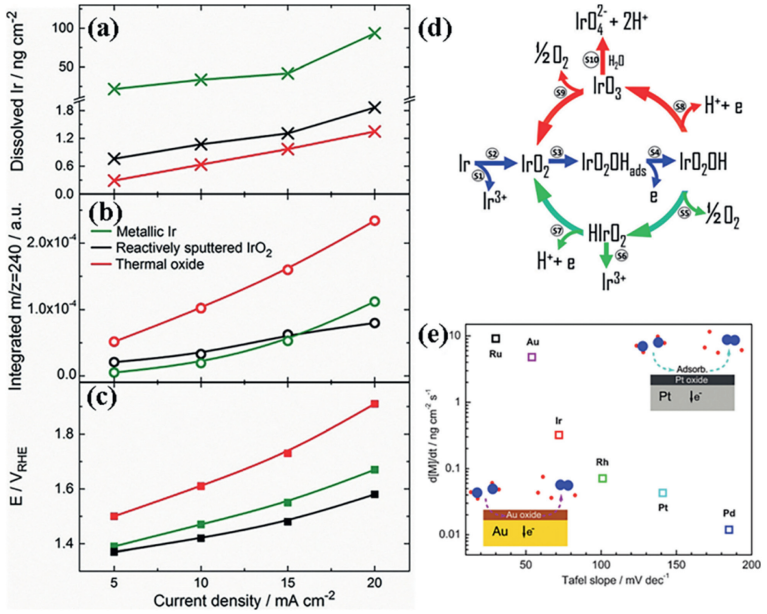

Fig. 2. Dependence of (a) the amount of dissolved Ir, (b) the formation of IrO_3, and (c) potential at the end of polarization on the current density obtained for metallic Ir (green), reactively sputtered IrO_2 (black) and thermal IrO_2 (red). (d) Universal mechanism correlating both the OER and dissolution pathways proposed by Kasian *et al.* Reproduced with permission [77]. Copyright 2018, Wiley. (e) Correlation between stability and the Tafel slope for the OER for the noble metals proposed by Cherevko *et al.* Reproduced with permission [81]. Copyright 2014, Wiley.

the following equation:

$$S-number=\frac{n_{O_2(OER)}}{n_{Ir(dissolved)}} \quad (10)$$

Here, $n_{O_2(OER)}$ and $n_{Ir(dissolved)}$ are the evolved O_2 molecules and dissolved Ir atoms, respectively. Though S numbers metrics relate the activity and stability from a macroscopic scope, it still lacks a detailed explanation for the trigger of the onset of OER and steady-state dissolution based on short-lived intermediates.

Further, Kasian *et al.* [77] designed a scanning flow cell (SFC) coupled with differential or online electrochemical mass spectrometry (DEMS/OLEMS) and inductively coupled plasma mass spectrometry (ICP-MS) to probe the transformation mechanism of intermediates and elemental dissolution. However, the authors did not get such a conclusion that activity and dissolution kept a reverse relationship. OER on the anodic reaction and oxidation of Ir sites were not inter-competing responses, meaning that activity and stability enabled to reach optimization in the meantime. For metallic Ir, reactively sputtered IrO_2 and thermally formed IrO_2, the authors [77] observed that O_2 molecules and IrO_3 formations and the dissolution of Ir atoms (Figs. 2a-c) were accompanied by the increase of current density. In contrast with thermally formed IrO_2, metallic Ir at the identical current density conditions delivered a higher dissolution, which was about two orders of magnitude than that of thermal oxide. Reversely, the detected potentials at the anode for metallic Ir were lower than that of thermally formed IrO_2 at the identical current density. For metallic Ir, low potentials, corresponding to low current density, triggered the domination dissolution of Ir atoms. In combination with the results from OLEMS, at the onset of OER, the polarization of Ir induces the formation of Ir^{III}, which is directly soluble. Subsequently, the soluble Ir^{III} is further oxidized as IrO_2, why metallic Ir shows a relatively high dissolution rate of Ir atoms. Of note, the soluble Ir^{III} formation is accompanied by the vacancy density, which is beneficial to the incorporation of oxygen atoms with the aid of applied potentials. Therefore, with the increasing coverage of oxide layers on metallic Ir, the formed IrO_2 phase becomes stable with high dissolution resistance. Similarly, reactively sputtered IrO_2 also shows such a reaction trend due to the formed IrO_x with low vacancy density. However, its activity and dissolution of Ir atoms are superior to that of metallic Ir.

Thermally formed IrO_2 with a rutile structure is ascribed to the second dissolution route [56,77–79]. In sharp contrast, the dissolution of Ir atoms is almost linearly related to current density, which is accounted for the formation of IrO_3 (Fig. 2d). thermally formed IrO_2 shows a low reactivity activity but a low dissolution. At the initial stage, water adsorption and further deprotonation at Ir active sites led to the formation of OH* species, which caused the oxidation of Ir center sites into $Ir^{V}O_2(OH)$ intermediates. Ir catalysts are considered as potential responses to activity and stability due to the charge-storing mechanism at Ir center sites. The further increase in potentials led to the formation of $Ir^{VI}O_3$ intermediates, which can be further decomposed as O_2 and IrO_2, or dissolved as IrO_4^{2-} species. Two universal dissolution routes can play a pivotal role in the whole OER, depending on the applied potentials, nature of catalysis and surface defects [73].

Corresponding to two dissolution routes of Ir atoms, the Tafel slope is also another vital parameter to reveal its reactivity route [73,80]. The high Tafel slope means that OER proceeds mainly *via* AEM, such as Pt and Pd catalysts (Fig. 2e), whose lattice oxygen is not involved in the transformation of intermediates [81]. On the contrary, a low Tafel slope corresponds to high reactivity activity, involving the participation of the surface oxide layer. In other words, the surface oxide layer is correlated with dissolved intermediates according to the two dissolution routes mentioned above. Besides OLEMS coupled with ICP-MS and the Tafel slope, other methods and techniques, such as *in situ* X-ray absorption spectroscopy (XAS) and cyclic voltammetry, are also helpful to detect the structural evolution and the transient transformation route of intermediates [82–85].

2.2.2. The key factors on catalysts for the dissolution of Ir atoms

Apart from operation conditions, the confirmation of the nature of catalysts is also a great contribution to understanding and promote the development of highly stable Ir catalysts with accepted activity. Intensive efforts have determined the effect of the nature of catalysts on the dissolution of Ir atoms, deciding which route is

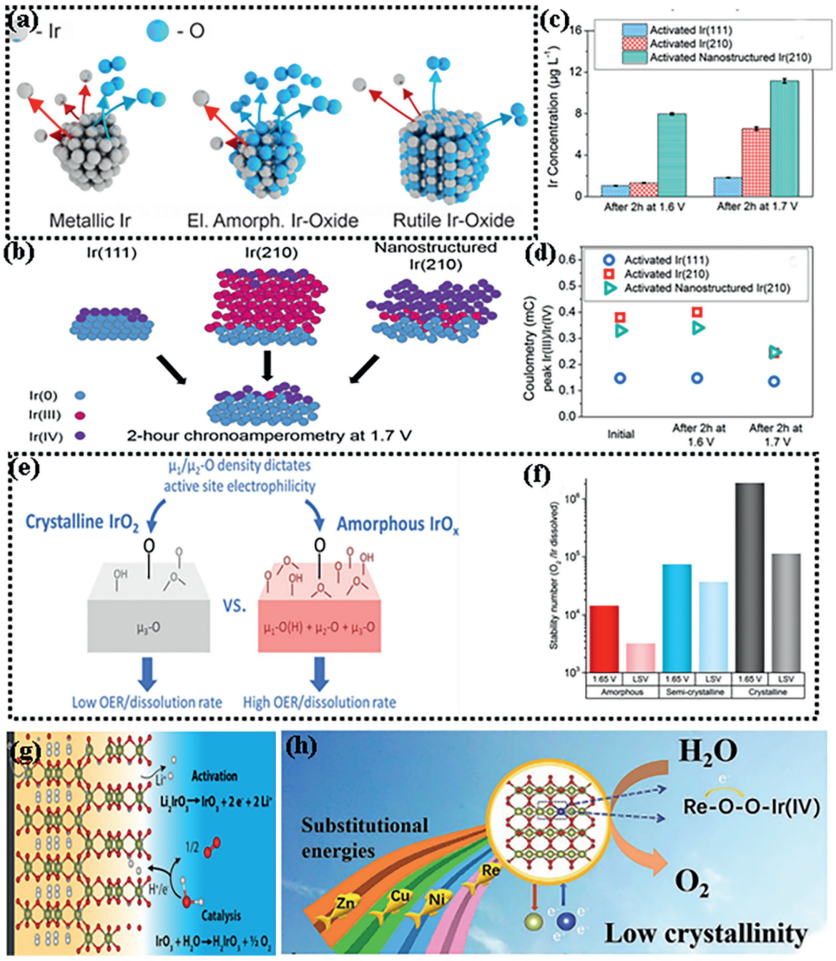

Fig. 3. (a) Models of metallic Ir, IrO_x and rutile IrO_2. Reproduce with permission [87]. Copyright 2017, American Chemical Society. (b) Oxidation route of metallic Ir with different crystal orientations, (c) Ir concentrations in the electrolyte and (d) Coulometry under the 0.9 V peak after electrochemical activation and after chronoamperometric steps at 1.6 and 1.7 V. Reproduce with permission [88]. Copyright 2019, American Chemical Society. (e) Schematic representation of the proposed operando structure–activity–stability relation and (f) stability numbers for IrO_x films on Si in 0.1 mol/L H_2SO_4, calculated from the potential holding data at 1.65 V RHE and LSV from 1.2 V RHE to 5 mA/cm^2 at 10 mV/s. Reproduce with permission [57]. (g) Cation exchange method for stable H_XIrO_3. Reproduce with permission [94]. Copyright 2019, American Chemical Society. (h) Re-dopped IrO_2 for suppressing Ir dissolution. Reproduce with permission [85]. Copyright 2023, Wiley.

an alternative for the transformation of intermediates and its dissolution mechanism [58,77,81,86].

As discussed above, the composition and crystallization of Ir-based catalysts enable to trigger different dissolution mechanisms of Ir atoms, namely direct dissolution, and overoxidation, respectively (Fig. 3a). Correspondingly, two dissolution routes are described as the following equation [87]:

Direct dissolution:

$$Ir \rightarrow Ir^{3+} + 3e^- \ (E = 1.156\,V + 0.019\log[Ir^{3+}]) \quad (11)$$

Overoxidation:

$$Ir_2O_3 + 5H_2O \rightarrow 2IrO_4^{2-} + 10H^+ + 6e^- \ (E = 1.680\,V - 0.0986\log pH + 0.0197\log[IrO_4^{2-}]) \quad (12)$$

Presumably, the essential reason for facing different dissolution routes for Ir-based catalysts is the difference in vacancy density on their surface [56]. In addition, the crystal orientation of metallic Ir is also pivotal to the activity and stability of OER [88]. Given morphologies, Ir(210) is atomically rougher than Ir(111) with the density of coordination atoms range as Ir(111) < Ir(210) < nanostructured Ir(210). Ir^{3+} atomic fraction on the surface after chronoamperometric steps decreased with the increase of applied potentials, and the quantity of dissolved Ir atoms was more evident at 1.7 V than at 1.6 V (Figs. 3b-d). Nevertheless, the Ir dissolution rate after chronoamperometric steps at 1.6 V was bigger than that at 1.7 V. Ir, Ir^{3+} and Ir^{5+} coexisted at the wide potential window, and the generated Ir^{3+} had a trend to be transformed into IrO_2 on the surface. This is also why nanostructured Ir(210) displayed a high Ir dissolution quantity in the electrolyte and high activity. Comparatively, low activity and Ir dissolution were observed on Ir(111). We can conclude that an outstanding catalyst should display an Ir dissolution with "neither too fast nor too slow". Ir^{3+} is also a bridged intermediate to relate activity and stability. At the initial stage, metallic Ir can generate abundant Ir^{3+}, which caused severe Ir dissolution. However, subsequent oxidation of Ir^{3+} into IrO_2 on the surface also contributes to high activity.

The deprotonation on and near the surface poses a vital effect on the transformation barriers of oxygen-containing intermediates and Ir dissolution [75,89–92]. Given soluble intermediates of $HIr^{III}O_2$, IrO_4^{2-} species and so on, water adsorption and incorporation are key processes to correlate stable IrO_x phase and Ir dissolution. IrO_x catalysts act as electrophilic agents, mainly O^{n-} functional groups [57,75], to accumulate electron holes for water attack. Subsequently, protonated IrO_x becomes a nucleophile for the following OER along with the deprotonation processes. Though hydrate IrO_x can effectively reduce the transformation barriers of

oxygen-containing intermediates, it enables to lower the coordination number of Ir atoms for high Ir dissolution. Mom *et al.* [57] designed a series of IrO_x with different amounts of μ_2–O moieties and μ_1–O/μ_2–O mixture for variations in deprotonation depth (Fig. 3) to modify the barriers of oxygen generation and Ir dissolution. The definition of μ_1–O is the coordinatively unsaturated sites on its surface and subsurface; μ_2–O corresponds to the bridged oxygen with two Ir atoms; μ_3–O is related to coordinatively saturated sites, commonly existing in the bulk. The various oxygen structures in IrO_x reveal that neighbored Ir will deliver a charge compensation for different types of oxygen atoms (Figs. 3e and f). Thus, μ_1–O and μ_2–O moieties can fasten the deprotonation processes for relatively low OER barriers, but a weak bridge between Ir and O atoms with high Ir dissolution.

Similar work was done by Grunwaldt *et al.* [56], who proposed a strategy of increasing Ir-Ir interaction *via* modulating oxygen vacancy of IrO_x. They observed that the increase of Ir-Ir interaction *via* the calcination of IrO_2 and oxygen removal was beneficial in promoting dissolution stability (Fig. 3g). Essentially, the increase of Ir-Ir bonds is still in the framework of modulating μ_1–O/μ_2–O mixtures on its (sub)surface for the trade-off between activity and stability. Nevertheless, the generated oxygen vacancy can be fulfilled by oxygen atoms of water molecules again, and thus the resulting fading in catalytic activity is ascribed to the reduced conductivity or the dissolution of Ir sites. It is suggested that the construction of stable oxygen vacancy is effective in simultaneously improving catalytic activity and stability. In addition, the formation of stable hydrate IrO_x, such as H_xIrO_3 [93] and H_xIrO_4 [94], is also an alternative route for its long-term operation, which was determined by Pearce and Perez *et al.* These hydrated IrO_x phases are characterized with abundant tunnels for proton insertion/extraction. The as-prepared hydrated IrO_x displayed high stability, which avoids direct coupling of protons from water incorporation with a certain volatility. These researches above mainly focus on the improvement of Ir dissolution resistivity, ultimately getting a balance between activity and stability. Indeed, the common phenomenon is the inverse relationship of activity and Ir dissolution, essentially ascribed as the modulation of electronic structures of Ir active sites. To promote activity and Ir dissolution resistivity in the meanwhile, partial replacement of Ir atoms of IrO_x catalysts is used to increase the interaction of Ir-M bonds, and the neighboring oxygen atoms around Ir active sites are activated for the water incorporation. Thus, it is promising to become active for IrO_x catalysts on the premise of low Ir dissolution. Yang *et al.* [85] utilized Re to dope IrO_2 in the form of Re-O_2-Ir bonds (Fig. 3h). The confined Re atoms enabled to suppression Ir dissolution *via* strong Re-Ir interaction. The authors announced that the hybridization orbits of Re 5d and O 2p bands were broadened for water attack and incorporation, thus exhibiting a low overpotential of 255 mV at 10 mA/cm^2 and maintained 170 h under acid solution. These works revealed that the modulation of electrical structures is a double-edged sword for activity and stability, which also shed light on Ir dissolution mechanism for breaking inverse relationship between activity and stability.

2.3. The strategies for stability and activity

Generally, the Ir leaching is involved in LOM, during which lattice oxygen participates in OER. Essentially, for LOM-involved oxides, O 2p orbitals may not form a hybridization orbital with d orbitals of metal, and thus the as-formed oxygen non-bonding orbitals are higher than M-O hybridization bands. When oxygen nonbanding orbitals are higher than the filled lower Hubbard band, these oxygen sites can act as redox centers for electron extraction. Further, accompanied by the generation of oxygen vacancy, exposed metal active sites become undercoordinated, tending to trap oxygen atoms and form a close catalytic cycle. However, undercoordinated sites can be also etched due to the charge equilibrium and compensation. It signifies that oxygen vacancy generation and oxygen filling are inter-competing for dissolution and dissolution of cations. The fast oxygen vacancy generation rate not only poses trouble to its stability but also suppresses its electrical conductivity. For relieving LOM-involved reactions, the confinement of active lattice oxygen sites and the increase of the formation energy of oxygen vacancy are the alternatives to lower oxygen nonbonding orbitals.

Compared with relatively high activity for Ir-based catalysts, its acid-stable property is more attractive. The dissolution of Ir-based materials still occurs when the applied potential is more than 1.6 V *vs.* RHE. In consideration of its scarcity and high price, it is urged to reduce the usage of Ir metal, thus introducing new elements or phases to favor its electrochemical performance. At the onset of OER, oxygen-containing species are absorbed on active sites, and meanwhile, the oxidation of Ir active sites occurs. This structural evolution is observed in other heteroatoms, which means that the individual heteroatoms also endure the strong acid and high oxidation state. As done by Nørskov *et al.* (Fig. 1d) [95], the descriptors of the Pourbaix decomposition free energy (ΔG_{pbx}) are used to evaluate the stability of metal oxide. Based on the high-through screening of Materials Project data, they identified 68 likely acid-stable candidates during the O_2 evolution process. Meanwhile, the elements of Sb, Ti, Sn, Ge, Mo and W can endure such harsh circumstances, signifying that they can be alternatives as doping elements or supported materials.

Besides, the conductivity in sluggish kinetics of multistep processes is also a grand challenge for highly effective O_2-evolution catalysis, which is vital to activity. On one hand, catalysts with high intrinsic conductivity are prepared *via* the choice of electrical supporters and elemental doping. Strasser *et al.* [96] used nanostructured Ir nano-dendrites supported on antimony-doped tin oxide (ATO) for efficient and stable water-splitting catalysts. ATO is reported as relatively high electronic conductivity, which can fasten electron transfer among Ir sites. Element doping is also a favorable strategy to adjust electronic structures and enhance their intrinsic conductivity. For perfectly latticed IrO_2, the stable coordination surroundings around Ir sites determine stable electron numbers, thus leading to a relatively weak electron transfer. The introduced heteroatoms can break such an electron equilibrium and donate electrons to active sites, thus enhancing the electron transfer and suppressing its over-oxidation [33]. On the other hand, a catalyst-coated membrane with high conductivity should be realized for a continuous conductive network, commonly *via* high Ir mass loading. Even if the catalysts can confer a high electrical conductivity, the weak contact resistance from the discontinuous Ir-based catalyst layer also consumes enormous energy. The authors [97] compared the role of a homogeneous and a thin, inhomogeneous IrO_2 catalyst on electronic contact in Figs. 1e-h. As shown in Fig. 1f, homogeneous IrO_2 catalysts (>1 $mg_{Ir}/cm^2{}_{MEA}$) delivered a high in-plane electronic conductivity, however, the inhomogeneous IrO_2 catalysts (<0.5 $mg_{Ir}/cm^2{}_{MEA}$) imparted some resistance from in-plane and cross-section. Further, they replaced the Ti porous transport layer with the carbon porous transport layer for superior electronic contact, whereas the carbon porous transport layer is easy to dissolve. Therefore, a homogenous Ir distribution technology needs to be developed for forming a continuous conductive layer with low Ir loadings.

Effective evaluation of catalytic activity for OER as well as their durability under operation is key to analyzing and understanding structural evolution and failure mechanism. Apart from ICP-MS coupled with DEMS for transient dissolution of active sites above, XAS enables to detection of the chemical state and electronic properties when it comes to determining the specific struc-

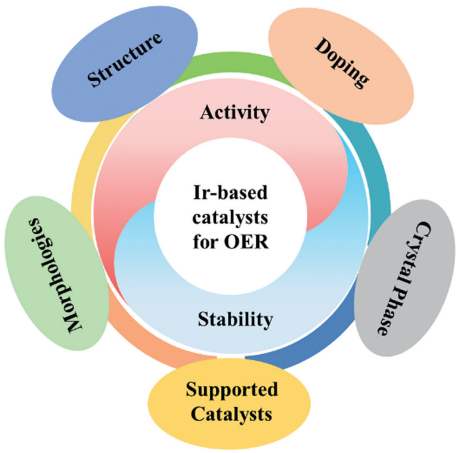

Fig. 4. The alternative methods for boosting the performance of Ir-based catalysts in terms of activity and stability.

ture change of water electrolysis catalysts under service conditions. XAS can present the fine structure information, including valent state and local coordination structure *via* X-ray absorption near edge (XANES), and the extended X-ray absorption fine structure (EXAFS), further deducing the electron transfer and identifying the real active sites. To provide the information of surface state under operation, near-ambient pressure X-ray photoelectron spectroscopy (nap-XPS), which can detect the atomic information at the catalysts/liquid interfaces under ~20 mbar of gaseous species, provides insight into the catalyst behavior under electrified condition for real operation. *In-situ* Raman spectroscopy is also a powerful tool to detect key intermediates as well as their evolution to reveal the catalytic routes. The oxygen evolution process is complex and needs various coupled characterization methods under operando conditions to demonstrate the structural information in real conditions, especially at their solid/liquid interfaces.

3. Ir-based electrocatalysts for OER

In consideration of the optimized trade-off between activity and stability, Ir-based catalysts are one of the most promising materials to be applied to practical water splitting. Nevertheless, its reserves and cost pose a grand challenge to the wide usage on water splitting. Thus, the common routes are to boost its activity and stability *via* structure optimization [94,98], morphological control [99–102], elemental doping [103,104], catalyst-supported regulation [105,106] and crystal phase design [107–109] as described in the following sections (Fig. 4). Accordingly, the intrinsic activity of Ir sites and anti-dissolution activity get improved. In the meanwhile, we summarize the status of Ir-based catalysts as listed in Table 1.

3.1. Structure optimization

IrO_2 has long been used as the benchmark to measure the activity and stability of catalysts for OER. Of note, metallic Ir will evolve into IrO_2 during OER, and thus more attention is paid to IrO_2 catalysts. As shown in Fig. 5a [110], the direct dissolution *via* $Ir(OH)_3$ occurred at the initial stage; alternatively, soluble IrO_3 due to the overoxidation is generated on high potentials. Indeed, the electronic structure of Ir active sites poses a vital role in suppressing soluble species and promoting the fast transformation of oxygen-containing intermediates. Both AEM and LOM are involved with OH* during OER. Shao *et al.* [111] used a robust synthetic route referred to as the "mechano-thermal" method for iridium metalline oxide (1T-phase-IrO_2) as shown in Fig. 5b. The X-ray diffraction (XRD) results in Fig. 5c showed that sharp Bragg diffractions at ~12.81° corresponded to the (0001) diffraction plane of 1T-IrO_2 phase with a layered structure along the c-axis. Based on the determination of an AA-stacked structure and an Ir-O_6 (2.00 Å) and Ir-Ir_6 coordination shell (3.12 Å) in the as-prepared 1T-IrO_2 catalyst, one can observe that Ir active sites on the surface were in the form of Ir^{3+} species. Hence, the accumulation of OH* at the initial stage on the interface of the 1T-IrO_2 catalyst was boosted, which effectively reduced the transformation barriers of subsequent OH* dissociation to O*. Presumedly, Ir^{3+} species on the surface can initiate the adsorption of OH* and break the limit of rutile IrO_2 on the penitential-limiting step of OH* to O* species. The authors claimed that the 1T-IrO_2 phase and a layered structure delivered the catalyst with a favorable performance (197 mV@10 mA/cm^2 and 45h@50 mA/cm_{geo}^2) (Fig. 5d). Though a detailed analysis of phase structure is displayed, an obvious difference in layered structure for 1T-IrO_2 also contributed to its oxygen evolution processes in comparison with rutile IrO_2. The layered structure formed a continuous conductivity network, beneficial to fast charge transfer among Ir sites. Thus, the specific phase structure and continuous conductivity network synergistically contributed to outstanding performance.

Similarly, Herranz *et al.* [112] explored the effect of surface Ir^{5+} on Ir oxides for O_2 evolution (Fig. 5e). IrO_2 catalysts, regardless of the oxide types, crystalline structure, and surface composites, underwent interfacial oxidation and were stabilized in the form of Ir^{5+} states. Meanwhile, the formed Ir^{5+} states were consistent with the onset of O_2 evolution, hinting at the involvement of Ir^{5+} states in the transformation of oxygen-containing intermediates. Further, Zou *et al.* [47] introduced Sr element into IrO_x for open-framework iridates. Metastable strontium iridates triggered the exchange of Sr^{2+} with H^+ ions and the structured rearrangement for open-framework IrO_xH_y (Fig. 5f). Such a formed structure was favorable to the oxidation of hydroxyls and the coupling of O–O bonds. Thus, the iridate maintained its catalytic activity for more than 1000 h at 10 mA/cm_{geo}^2. Actually, defect density [56,74], oxygen types [40,57], and joint types of unit cell [40,93,94,107] pose the key roles on the O_2 evolution kinetics and stability of Ir-based catalysts.

3.2. Morphological control

Active site density and electronic conductivity are two important factors for the fast kinetics of oxygen evolution process [100,113–116]. Essentially, OER is a proton-coupled electron transfer process, strongly dependent on the synthetic effect of proton and electron kinetics [117–119]. Commonly, morphological control is a favorable choice to boost the catalytic performance of Ir-based materials, presumably *via* exposing more active sites for fast proton kinetics [21,120,121]. Additionally, the manipulation of morphological structures constructs an electron transfer tunnel for high in-plane conductivity in catalytic layers, thus lowering the ohmic resistance among catalysts. Nowadays, various morphologies are proposed, such as zero-dimensional nanoparticles [122,123], one-dimensional nanowires [124,125], two-dimensional nanosheets/nanotubes/nanorods [38,39,126,127], and porous structures [128,129].

Mohamed *et al.* [130] dispersed IrO_x nanoparticles (IrO_x NPs) on tin-doped indium oxide (ITO) for forming IrO_x NPs with high active surface areas (Figs. 6a and b). Two challenges exist in the preparation of IrO_x NPs, namely the severe aggregation and growth of nanoparticles and the choice of conductive and cheap support materials with high corrosion resistance [131]. Mohamed *et al.* revealed that the coverage of IrO_x NPs on ITO (the distances of IrO_x NPs) was reversely related to activity. The as-prepared IrO_x NPs

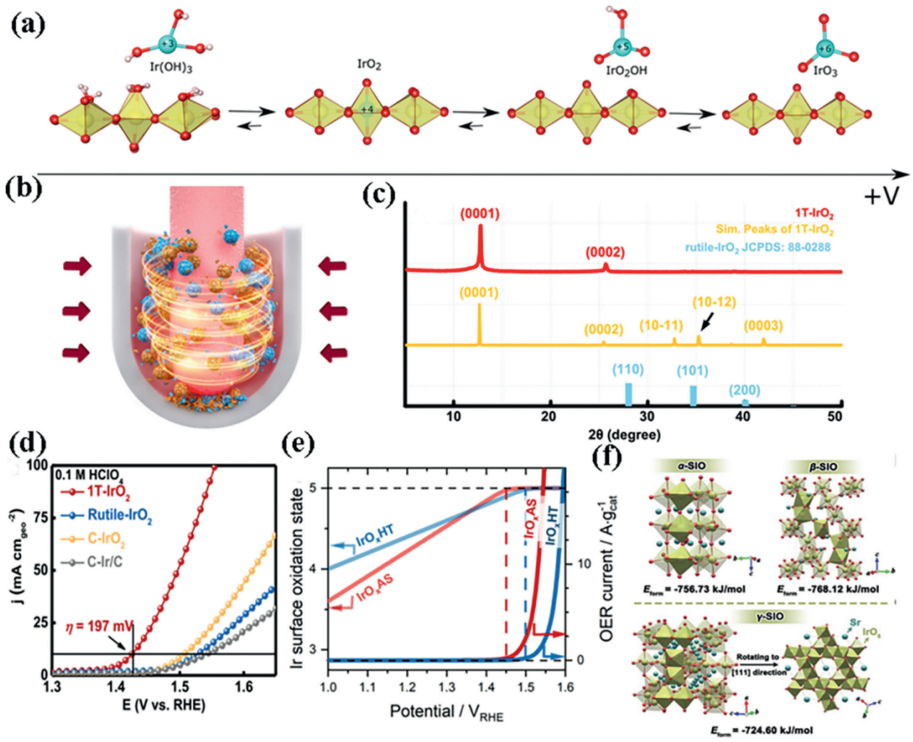

Fig. 5. (a) The Ir dissolution mechanisms. Reproduce with permission [110]. Copyright 2020, American Chemical Society. (b) Schematic representation of the mechano-thermal reactor for preparing 1T-IrO_2, where the mechanical and thermal operations are controlled simultaneously. The blue and yellow balls indicate $IrCl_3$ and KOH, respectively. (c) Comparison of XRD patterns of 1T-IrO_2 (red curve), simulation X-ray diffraction peak (yellow curve) of 1T-IrO_2 and the rutile-IrO_2 (blue line) (JCPDS No. 88–0288). Reproduce with permission [111]. Copyright 2021, The Author(s). (d) Polarization curves of 1T-IrO_2, Rutile-IrO_2, and commercial catalysts (C-IrO_2 and C-Ir/C) in O_2-saturated 0.1 mol/L $HClO_4$ electrolyte with iR-correction. (e) Polarization curves and Ir surface oxidation state with the evolution of applied potential. Reproduce with permission [112]. (f) Crystal structures of α-SIO, β-SIO, and γ-SIO. Reproduce with permission [47]. Copyright 2023, Wiley.

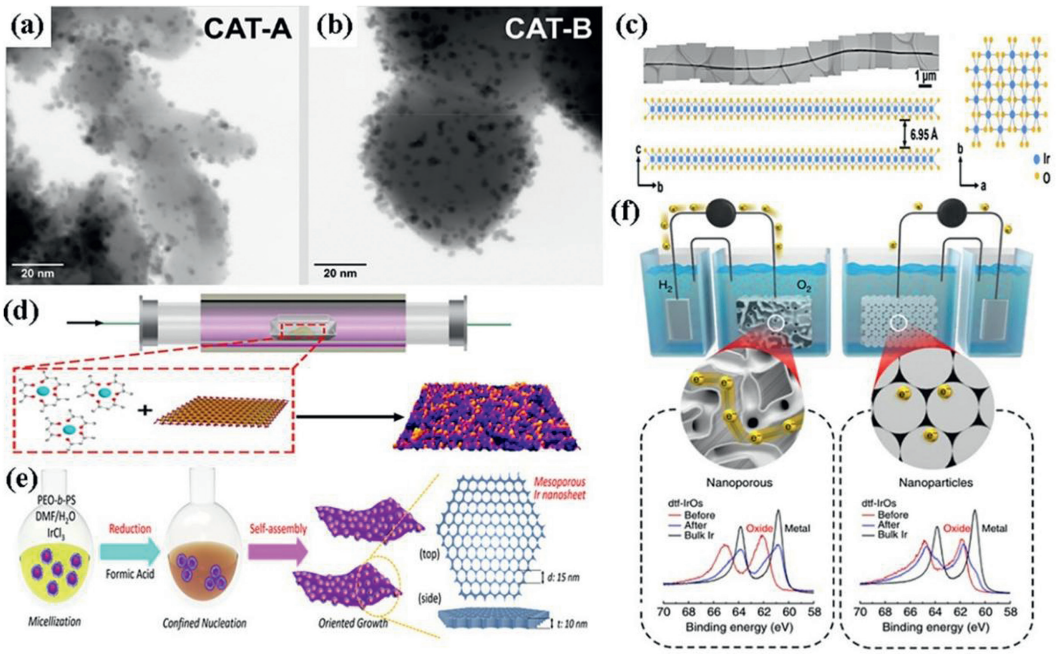

Fig. 6. High magnification HR-STEM micrographs of (a) CAT-A and (b) CAT-B. Reproduce with permission [130]. Copyright 2023, American Chemical Society. (c) Pictorial illustration of the crystal structure for the IrO_2NR. Reproduce with permission [132]. Copyright 2023, The Author(s). (d) Schematic illustration of the general synthetic process for amorphous noble metal NSs. Reproduce with permission [38]. Copyright 2019, The Author(s). (e) Formation mechanism of the mesoporous Ir nanosheets. Reproduce with permission [133]. Copyright 2018, American Chemical Society. (f) Schematic illustrates the impact of multiple oxide-oxide interfaces (present on dnp-$Ir_{50}Os_{50}$ electrodes) on conductivity. Reproduce with permission [101]. Copyright 2017, The Author(s).

Table 1
The performance of Ir-based catalysts for OER.

Catalysts	Electrolyte	Scan rate (mV/s)	Overpotential (mV)@10 mA/cm^2	Tafel slope (mV/dec)	Ref.
ZnNiCoIrMn	0.1 mol/L $HClO_4$	5	237	46	[22]
Ir-MnO_2	0.5 mol/L H_2SO_4	1	218	59.61	[33]
6H-$SrIrO_3$	0.5 mol/L H_2SO_4	0.5	248	–	[36]
Amorphous Ir NSs	0.1 mol/L $HClO_4$	5	255	40	[38]
IrO_2	0.1 mol/L $HClO_4$	5	373	112	[38]
RuIr-NC	0.5 mol/L H_2SO_4	5	165	42.8	[39]
H-γ-SIO-1	0.1 mol/L $HClO_4$	10	200	60	[47]
$Pr_3Ir_{1-x}Mo_xO_7$	0.1 mol/L $HClO_4$	5	259	50.52	[51]
a-PN-IN frame/C	0.1 mol/L $HClO_4$	5	308	47.49	[79]
Li-IrO_x	0.5 mol/L H_2SO_4	10	290	39	[86]
Ir NPs	0.5 mol/L $HClO_4$	5	290	51.4	[116]
sl-$Mn_{0.98}Ir_{0.02}O_2$	0.5 mol/L H_2SO_4	1	280	147	[120]
Ir-Co_3O_4	0.5 mol/L H_2SO_4	5	236	52.6	[122]
Ir nanosheets	0.5 mol/L H_2SO_4	5	240	49	[133]
Ir_2Sm NPs	0.5 mol/L H_2SO_4	5	275	72.9	[135]
$Ir_{0.83}Sn_{0.17}O_2$	0.5 mol/L H_2SO_4	5	284	54.2	[137]
$Ir_{0.06}Co_{2.94}O_4$	0.1 mol/L $HClO_4$	5	300	45	[138]
Plasma-oxidized IrO_2	1 mol/L H_2SO_4	20	280	85	[139]
IrO_x/Ti	0.5 mol/L H_2SO_4	5	254	48	[141]
$Ru_{0.5}Ir_{0.5}O_2$	0.5 mol/L H_2SO_4	5	151	45	[142]
Ag_1/IrO_x SAC	0.5 mol/L H_2SO_4	–	224	50.43	[143]
GB-$Ta_{0.1}Tm_{0.1}Ir_{0.8}O_{2-\delta}$	0.5 mol/L H_2SO_4	5	198	64	[144]

reached 1.525 V *vs.* RHE at the current density of 207 ± 34 A/g_{Ir}. One/two-dimensional and porous nanostructures remain interconnected for efficient electron/proton transfer, attracting much attention. Shao and his colleagues [132] designed IrO_2 nanosheets with a nanoribbon structure using the molten-alkali mechanochemical method (Fig. 6c). Such a nanosheet structure exposed abundant active sites, especially at the edges, which enabled to manipulate the adsorption of O* intermediates (rate-determining step) for the optimal adsorption binding of oxygen-containing intermediates. And the electrical transport tunnels along nanosheets conferred a high electrical conductivity. The two synthetic factors of active sites and electrical conductivity delivered IrO_2 nanosheets with an overpotential of 205 mV at 10 mA/cm^2 and a high stability for 500,000 s. Additionally, Li and his group [38] constructed amorphous Ir nanosheets *via* direct anneal (Fig. 6d), effectively improving its mass activity as high as 2.5 and 17.6 times corresponding to crystalline Ir nanosheets and commercial IrO_2 catalysts, respectively (Fig. 6b). On the exploration of two-dimensional nanosheets, Yamauchi *et al.* [133] introduced mesopores into the plane of IrO_2 nanosheets for unique electronic transport properties and high specific surface areas (Fig. 6e). They used diblock copolymer (poly(ethylene oxide)-*b*-polystyrene, PEO-*b*-PS) micelles as a template to induce the assembly of Ir nanosheets. Hence, the mesoporous Ir nanosheets displayed an overpotential of 240 mV at 10 mA/cm^2 and a service lifetime of over 8 h at 10 mA/cm^2. Though two-dimensional structures can reduce the contact resistance as they can, the interfacial contact is still improved *via* further morphological manipulation. In the meanwhile, two-dimension structures impose restrictions on water/gas transfer, especially at high current density, which will retard the reaction kinetics, even at the premise of high active site density and high conductivity. Kim *et al.* [101] dissolved Os element of $Ir_{25}Os_{75}$ alloy to form a porous Ir/IrO_2 with three-dimensionally interconnected structure (Fig. 6f). It still maintained the integrity of the catalyst layers for a low resistance electron transport, especially in the cross sections of catalyst layers. They observed that carrier mobility governed the conductivity, which can be controlled *via* the morphologies of $Ir_{25}Os_{75}$ alloy (conductivity: $Ir_{50}Os_{50} < Ir_{25}Os_{75}$); nonetheless, its activity was boosted *via* the dealloying of Os of $Ir_{25}Os_{75}$ alloy due to the increasingly exposed active sites. Thus, they realized a trade-off between activity and conductivity *via* morphology control, achieving a ~8-fold improvement in activity-stability factor (the ratio between activity for OER and stability of the oxide materials) relative to $Ir_{25}Os_{75}$ alloy.

3.3. Elemental doping

Though Ir-based catalysts keep a balance between activity and stability, Ir active sites still have the disadvantages of the inappropriate adsorption binding of oxygen-containing intermediates and weak anti-dissolution ability [134]. The introduction of heteroatoms into Ir-based catalysts can inherit its partial properties to offset intrinsic activity, electrical conductivity and durability ability [103,135–138]. The electronic structure in d bands is able to affect the adsorption ability of oxygen-containing intermediates. Ideally, when the electron number of anti-bonding e_g orbitals in the d band is close to 1 [54], it is the most favorable for the adsorption energies of the key intermediates. Upon the transformation of key intermediates, in the meanwhile, Ir atoms can be oxidized, even overoxidized, thus leading to severe Ir leaching [139]. Thus, the heteroatoms can play a key role in modulating the electronic structures of neighbored Ir atoms, or/and offsetting partial electrons to neighbored Ir atoms with low dissolution. Yang *et al.* [140] introduced Cu into IrO_2 for modulating d orbital occupation of IrO_2 with an effective improvement of oxygen evolution reaction activity. As Cu was doped, the d_{xy} orbital occupied states for Ir atoms were uplifted. Correspondingly, its antibonding orbitals of d_{z2} bands were shifted to a lower energy level. In the meanwhile, its d_{xz} and d_{yz} bands crossed the Fermi level, pushing partial electrons to d_{z2} orbital-occupied states, namely e_g number of ~ 1 for Ir atoms. An e_g orbital with an occupation of 1 electron facilitates the electron overlap between oxygen-containing intermediates and catalysts. Therefore, the optimized e_g occupation states delivered a low rate-determining step barrier with a high OER activity.

In comparison with crystalline IrO_2, Li-dopped IrO_x, namely amorphous Li-IrO_x, possessed higher oxidation states along with shrinkage in Ir-O bonds (Fig. 7a). The formed IrO_6 octahedrons in Li-IrO_x became electrophilic to lower the barriers of O_2 evolution. Li-IrO_x thus achieved a potential of 270 mV@10 mA/cm^2 and a stable operation time of 10 h. Furthermore, to concurrently boost intrinsic activity and stability, the Ti introduction into IrO_x for abundant Ir-O-Ti motifs enabled to transport electrons from Ti to Ir (Fig. 7b) [141]. It not only manipulated the electrical arrangement of Ir sites for the optimal adsorption of key interme-

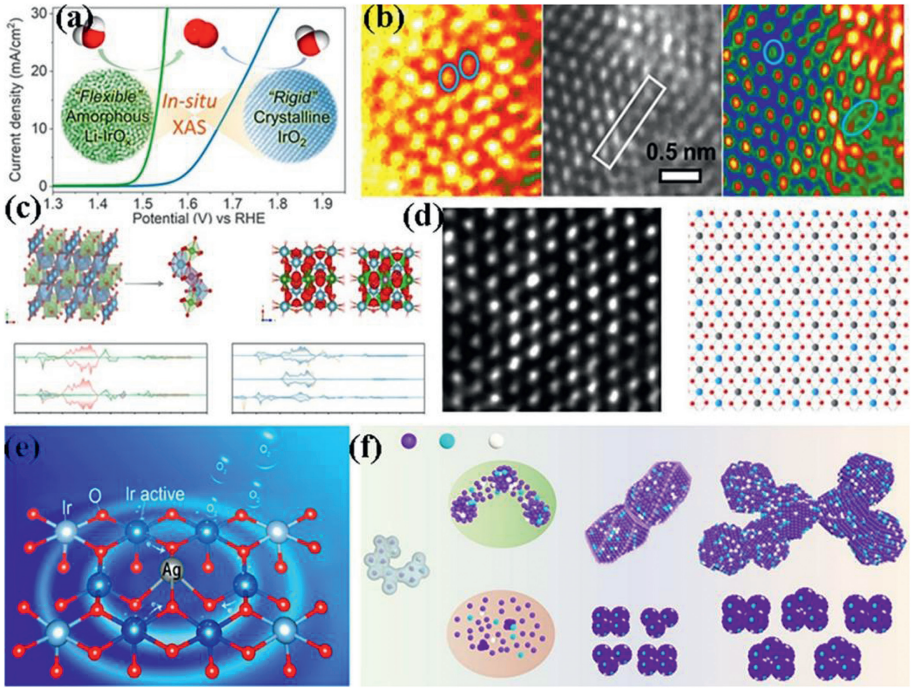

Fig. 7. (a) LSV curves of rutile IrO_2 and amorphous Li-IrO_x at 1 mV/s. Reproduce with permission [86]. Copyright 2019, American Chemical Society. (b) The morphological structure of Ti-IrO_x. Reproduce with permission [141]. Copyright 2023, Elsevier. (c) Crystal structures of Pr_3IrO and Mo-doped Pr_3IrO_7 along with the corresponding PDOS. Reproduce with permission [51]. Copyright 2023, The Author(s). (d) High-magnification image of $Ru_{0.5}Ir_{0.5}O_2$ and its schematic atom structure. Reproduce with permission [142]. Copyright 2023, The Author(s). (e) The model of Ag/IrO_x catalyst. Reproduce with permission [143]. Copyright 2021, American Chemical Society. (f) The schematic routes for synthesizing GB-$Ta_{0.1}Tm_{0.1}Ir_{0.8}O_{2-\delta}$ nanocatalyst *via* fast pyrolysis (top) *versus* nanoparticles without GB *via* slow pyrolysis (bottom). Reproduce with permission [144]. Copyright 2021, Springer Nature.

diates but also relieved the overoxidation of Ir sites *via* the electron offset. Thus, the Ti atomic doping into IrO_x/Ir led to 3.6-fold and one-order-magnitude improvement in terms of intrinsic activity and stability with a mass loading of 1.4 mg/cm^2. Similarly, Zou *et al.* [51] introduced Mo into Pr_3IrO_7 (Fig. 7c). The doped Mo fastened the leaching of Pr for easy surface construction and offset the charge depletion of neighbored Ir atoms. In the meanwhile, the formed Ir-O_{bri}–Mo species acted as strong Brønsted acidity to fasten the deprotonation of oxo intermediates. Thus, the optimal catalysts reached 10 mA/cm$_{geo}$^{2} with an overpotential of 259 mV, lower than that of the undoped counterpart (309 mV), and long stability of over 200 h with a mass loading of 0.25 mg/cm^2$_{geo}$. To further pursue a high catalytic activity, Shao *et al.* [142] designed two-dimensional Ru-Ir oxide, which delivered an overpotential of 151@10 mA/cm^2 with a mass loading of ~283 μg/cm^2 (Fig. 7d). In such a Ru-Ir oxide, the high oxidation state of Ru was observed to pre-store charge in order to trigger OER at the relatively low applied voltages. For the same purposes as Ru-Ir oxide above, Du *et al.* [143] used the direct oxidation of IrAg alloy to form Ag/IrO_x single-atom catalysts (SAC) (Fig. 7e). The Ag atoms in Ag/IrO_x SAC had two roles, namely pre-oxidizing Ir^{x+} ($x > 4$) and preventing the participation of lattice oxygen into O_2 evolution. Therefore, the prepared Ag/IrO_x SAC delivered an overpotential of 224 at 10 mA/cm^2 and durability over commercial Ir. On account of the effect of rare-earth elements on Ir-based catalysts, Jin *et al.* [144] compared the pyrolysis rate to induce a torsion strain between grain boundaries (GB) (Fig. 7f). One could observe that the induced torsion strain and ligand effect from the doped Ta and Tm atoms led to the favorable modulation of the Ir electrical structure for appropriate adsorption energy of key intermediates. Thus, the catalysts delivered an overpotential of 198 mV@10 mA/cm^2 and operated stably at 1.5 A/cm^2 for 500 h at the mass loading of 0.2 mg/cm^2. Indeed, heteroatoms can module electronic structure of Ir sites for favorable OER, however, the considerable challenge is the durability of heteroatoms under service conditions. And, its stability mechanism is confusing and attracts little attention.

3.4. Catalyst-supported regulation

The challenge of O_2 evolution catalysts has long been the cost of favorable Ir catalysts due to their scarcity and the activity related to intrinsic activity and active site density. Two alternative routes provide a solution to reduce the anodic cost: developing the alternatives to Ir-based catalysts and reducing the mass loading of Ir-based catalysts. Thus, to date, enormous efforts have been developed for the improvement of intrinsic activity and active site density of Ir-based catalysts for low Ir loadings [34,97,102,124,128,130]. To pursue highly exposed active sites, self-standing nanomaterials tend to agglomerate, posing some contradiction between exposing enough active sites and forming stable nanostructures [145–147]. The choice of supported Ir-based catalysts is favorable to well disperse Ir-based nanomaterials, allow flexible electron transfer between Ir sites and supports and relieve the dissolution of Ir atoms [148]. Nevertheless, operating conditions bring some trouble to supporters, asking for a high electrical conductivity and anti-corrosion ability [7,8,149].

Ge *et al.* [150] anchored Ir nanoparticles on Nb_2O_{5-x} (Ir/Nb_2O_{5-x}) as a model catalyst (Fig. 8a). One could observe that the optimal Ir/Nb_2O_{5-x} reached a current density of 10 mA/cm^2 at the low potential of 1.448 V *vs.* RHE, far lower than the counterpart of Ir NPs (1.515 V *vs.* RHE) (Fig. 8b). Direct spectroscopic evidence displayed that the average valence states of Nb decreased initially and increased subsequently with the increase of applied potential, with the counterpart Ir atoms increasing (Fig. 8c). In the initial step, the high valence states of Ir atoms *via* the electron interaction between Ir and Nb atoms triggered the fast O_2 evolution reaction at the relatively low potential. Further, the oxidation of Nb atoms transferred electrons to offset Ir atoms at high potential, which

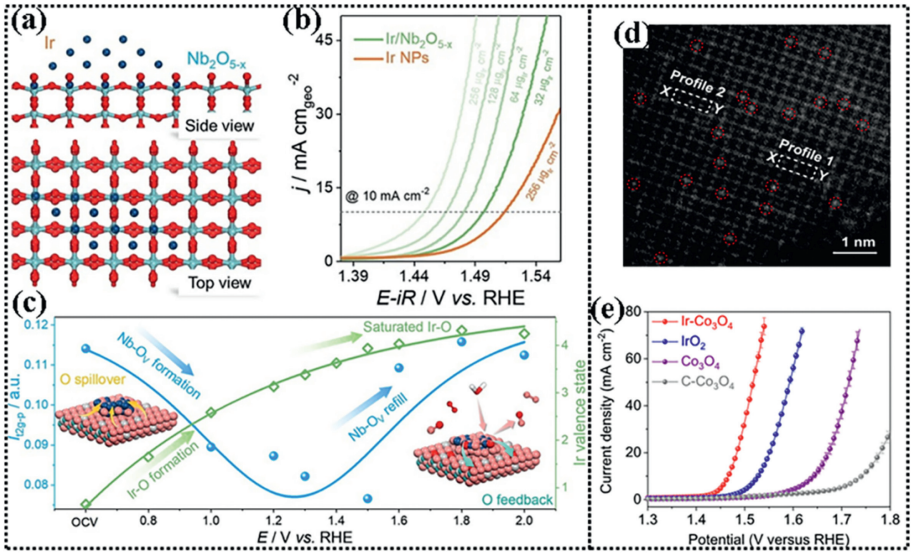

Fig. 8. (a) Schematic structure of Ir/Nb_2O_{5-x}, (b) normalized LSV curves of Ir/Nb_2O_{5-x}, and (c) illustration of the overall dynamic interface effect of Ir/Nb_2O_{5-x}. Reproduce with permission [150]. Copyright 2022, Wiley. (d) The morphological structure of Ir-Co_3O_4. (e) Polarization curves of Ir-Co_3O_4, IrO_2, Co_3O_4, and C–Co_3O_4 in 0.5 mol/L H_2SO_4 at a scanning rate of 5 mV/s. Reproduce with permission [122]. Copyright 2022, The Author(s).

prevented the overoxidation of Ir atoms for high anti-dissolution ability. Additionally, Ma *et al.* [122] used a mechanochemical approach to incorporate Ir single atoms into Co_3O_4 (Ir-Co_3O_4) as shown in Fig. 8d. It was found that Ir atoms were partially oxidized as active $Ir^{>4+}$ species. The formed Ir-O-Co bonds were electrophilic for key intermediates. As a result, Ir-Co_3O_4 exhibited an outstanding performance (236 mV@10 mA/cm^2) with a mass loading of 0.255 mg/cm^2 (Fig. 8e). Based on the light of supported Ir nanoparticles and single atoms, it is worth considering the effect of supporters and Ir-based nanomaterials on the activity and electron transfer between Ir atoms and supporters [151]. For example, M^{n+}/M^{n+1+} supporters are promising to allow the dynamic transfer to modulate the electron arrangement of Ir atoms; the intrinsic conductivity of supporters enables to fasten the electron transfer between supporters and Ir atoms; the distribution of Ir nanomaterials, such as core-shell structures, imposes a play on its conductivity, further its activity.

3.5. Crystal phase design

The benchmark of IrO_2 for OER catalysts still has much improvement in terms of activity and stability. The Ir-based perovskite and pyrochlore catalysts contain double metal sites, which can adjust the electronic structures of neighbored Ir atoms for favorable adsorption energy of key intermediates [152–154]. Possibly, the formed Ir-O-M unit cells in perovskite and pyrochlore assist the fast response to key intermediates and avoid forming direct Ir^{3+} for low Ir dissolution. Meanwhile, the incorporation of other metal atoms can effectively reduce the mass loading of Ir metals.

The perovskite structure (ABO_3) possesses double metal atoms, among which A is a rare-earth or alkaline-earth metal ion, and B is occupied by transition metal ions [155]. Zou *et al.* [36] constructed 6H-$SrIrO_3$ catalysts with face-sharing octahedral dimers, thus maintaining a highly stable structure under an acid solution (Fig. 9a). Benefiting from weakened surface Ir-O binding for low transformation barriers of O* to OOH* due to face-sharing octahedral dimers (Figs. 9b and c). Such 6H-$SrIrO_3$ catalysts effectively reduced 27.1 wt% iridium, but a 7-fold improvement in Ir mass activity in comparison with IrO_2 catalysts (Fig. 9d). Apart from 6H-$SrIrO_3$, Zou *et al.* [156] also explored the effect of triple perovskites on O_2 evolution (Fig. 9e). B sites in $Ba_3M'M''_2O_9$ structure contained two types of coordination environments: isolated $M'O_6$ octahedra and face-shared M''_2O_9 octahedral dimers. Obviously, there was a weak interaction between Ir atoms for $Ba_3TiIr_2O_9$, determined by Figs. 9f and g. Thus, TiO_6 octahedra enabled to modulate the covalency of Ir-O bonds; and face-sharing Ir_2O_9 octahedral dimers assisted the stability of Ir sites. The activity of $Ba_3TiIr_2O_9$ catalysts was about 10 times than that of IrO_2 (Fig. 9g). Similarly, R positions of Pyrochlore iridates ($R_2Ir_2O_7$) can be occupied by alkaline earth and rate earth metal ions, among which R also affects the electronic structure of neighbored Ir atoms. Zeng *et al.* [157] tried to explore the effect of R ionic radius on the intrinsic activity of pyrochlore iridates. One observed that the increased R ionic radius weakened electron interaction between iridate oxides, thus promoting Ir-O bond covalency for high O_2 evolution kinetics.

4. Applications in pemwe

The commercial PEMWE stack (Fig. 10a) is mainly the device for practical water splitting, which is made up of a single PEMWE cell as shown in Fig. 10b. Despite performance discrepancy in assembling a single PEMWE cell into a PEMWE stack, a single PEMWE cell is still pursuing high electrochemical performance with low contact resistance, fast mass transfer, and high stability, which can be affected by its main components of the catalysts-coated membrane (CCM) with anode and cathode materials, porous transport layers (PTLs), bipolar plates (BPPs) and gaskets (Fig. 10c) [158]. A single PEMWE cell is assembled *via* the sequence of BPPs, gaskets, PTLs, CCM, PTLs, gaskets, and BPPs (Fig. 10b). The CCM is the core of PEMWE, in charge of the catalytic performance of water splitting. Commonly, anode and cathode catalysts are sprayed or hot-pressed on both sides of the proton exchange membrane, namely CCM [8]. Alternatively, the catalysts are directly deposited on PTLs, which is necessary to adjust the pore size of PTLs with catalysts for optimal mass transfer. Upon operation, pure water is fed on the anode, where water is oxidized into O_2 molecules, protons and electrons. Subsequently, these electrons are transported to the cathode electrode *via* an external circuit. Meanwhile, the generated protons are diffused to the cathode electrode through the proton exchange membrane. Therefore, the combination of protons and electrons at the cathode electrodes leads to H_2 generation. During PEMWE operation, the accumulated O_2 and H_2 molecules can be exported and

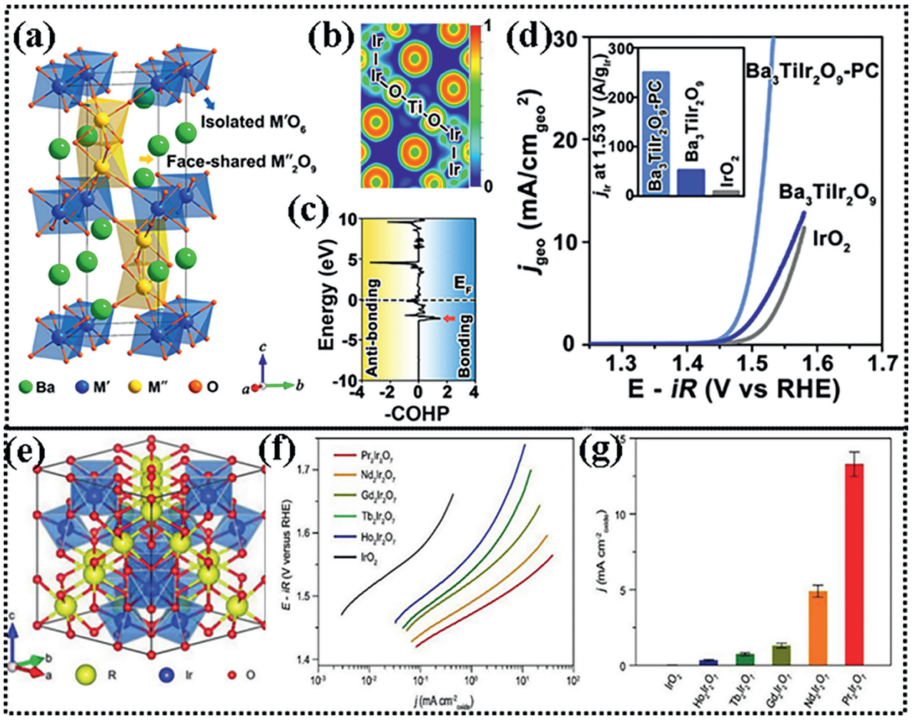

Fig. 9. (a) Crystal structure of $Ba_3M'M''_2O_9$. (b) Plot of ELF for $Ba_3TiIr_2O_9$. (c) COHP of the Ir−Ir bond in $Ba_3TiIr_2O_9$. (d) Their corresponding LSV. Reproduce with permission [156]. Copyright 2020, American Chemical Society. (e) The crystal structure of $R_2Ir_2O_7$. (f) The specific OER activity of $R_2Ir_2O_7$ and IrO_2 and (g) the corresponding specific OER activity at $\eta = 300$ mV. Reproduce with permission [157]. Copyright 2018, Wiley.

Table 2
Key performance of Ir-based anode catalysts in PEMWE.

Catalysts	Loadings (mg/cm^2)	Voltage (V@A/cm^2)	Stability (h@A/cm^2)	Temperature (°C)	Ref.
Ir-ND/ATO	1	1.80@1.5	/	80	[96]
IrOX/Zr2ON2	0.4Ir	1.927@2	50@1	/	[106]
Ti-IrOX/Ir	0.5	1.774@2	220@2	80	[141]
GB-TaxTmyIr1-x-yO2-δ	0.2	1.766@1, 1.868@1.5, 1.935@2	500@1.5	50	[144]
Sr2CaIrO6	0.4Ir	2.4@6	450@2	80	[155]
Ir	2	1.568@1 1.651@2	/	80	[162]
Ir88Ru12@CM	1	/	120@1	90	[163]
Ir AC/NN	1	1.82@3	90@3	80	[164]

collected *via* PTLs to fasten their mass transfer. Given the PEMWE system, the polarization curves are acceptedly used to describe the required potentials for water splitting *via* IR compensations with reasonable simplifications [8]:

$$V = E_{cell} + V_{act,c} + V_{act,a} + IR \quad (13)$$

where V, E_{cell}, $V_{act,c}$, $V_{act,a}$, I and R correspond to the electrolyzer voltage, open circuit voltage, cathode overpotentials, anode overpotentials, current density and ohmic resistance, respectively. Water splitting is an energy-uphill process, and E_{cell}, $V_{act,c}$ and $V_{act,a}$, related to the nature of anode and cathode catalysts, attract wide attention. Nonetheless, the factor of ohmic-resistance-induced voltage drop also plays a grand role in the required potentials at the electrolyzers. Of note, the model above is solely based on the analysis of the electrical contribution of individual modules at PEMWE, and further mass transport, including fed water, proton, and O_2/H_2 molecules, also suppress water splitting, especially at high current density [97,159–161]. Table 2 shows some key parameters of the Ir-based anode for PEMWE.

To push the application of PEMWE based on Ir-based catalysts at the anode, the reduction of Ir loadings is imperative. Nowadays, Ir loading for anode catalysts is as high as ~2 mg_{Ir}/cm^2, but feasible Ir loadings should be reduced to below ~0.5 mg_{Ir}/cm^2 when maintaining its activity and lifetime [162–164]. For a reduction of Ir loadings to such a degree, however, the formed isolated particles/clusters prevent the electron transfer among Ir-based catalysts and Ir-based electrodes from keeping much contact with PTLs. Thus, the extra potentials need to be applied to overcome the barrier of electron transfer among the whole PEMWE system. Intuitively, the phenomenon, namely maintaining its activity and successive conductive layers, are contradictory when reducing its Ir loadings. For unsupported catalysts, optimizing and increasing the activity are still common routes to reduce Ir mass loadings, such as structural optimization, morphological control, element doping, and crystal phase design. For supported catalysts, it is a prerequisite for acid-stable supports to well disperse Ir metals. Besides, one promises that supports are conductive and pose metal-support interaction for enhancing its activity with the modulation of local structure and active sites. Gasteriger *et al.* [165] suggested constructing a relatively high pack density of the Ir catalytic layer with an equivalent activity (Figs. 10d and e). Based on their specific surface area, the specific surface area of P2X catalysts was ~50 m^2/g,

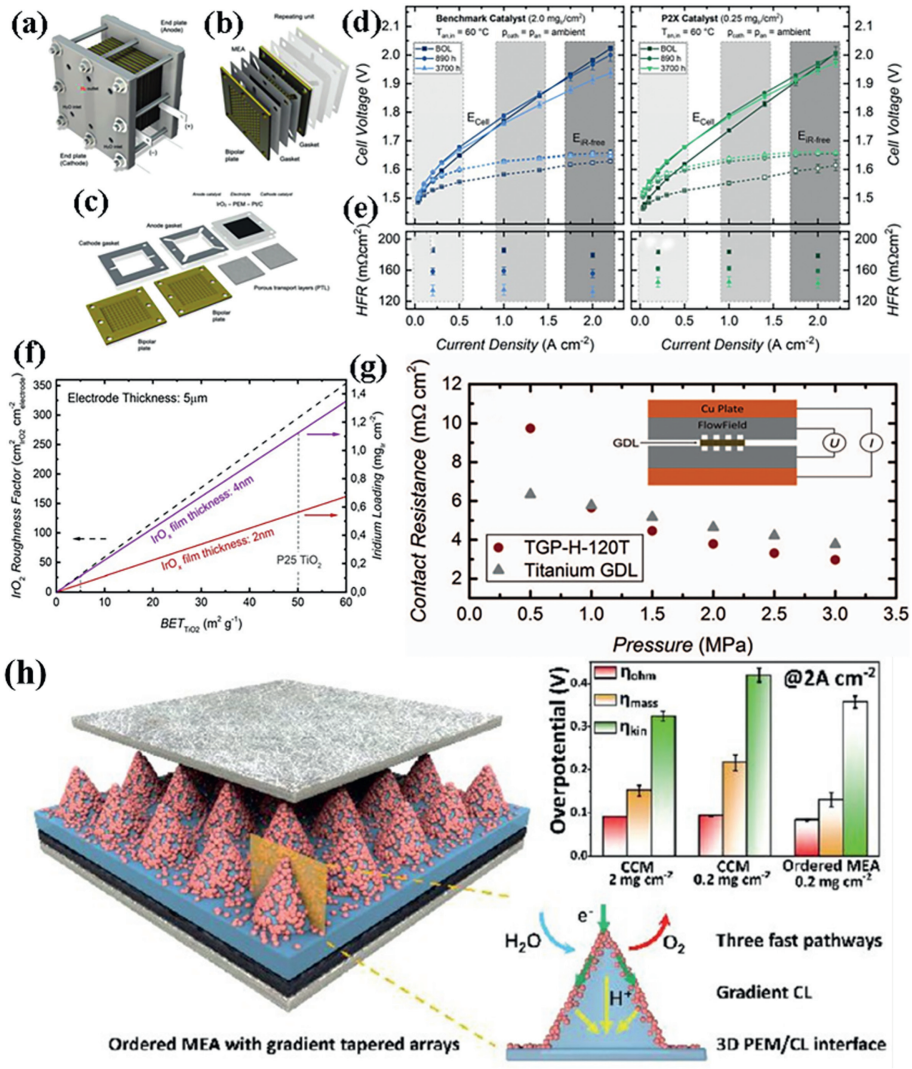

Fig. 10. Schematic drawings of (a) commercial proton exchange membrane water electrolysis (PEMWE) stack, (b) repeating unit cell, and (c) cell components. Reproduce with permission [158]. Copyright 2023, American Chemical Society. (d) Averaged polarization curves of the MEAs with the Benchmark anode catalyst and (e) its averaged HFR values and standard deviation determined from impedance measurements for all cells at three different current densities. Reproduce with permission [165]. Copyright 2022, The Author(s). (f) Projected iridium loading of a 5 μm electrode (right-hand y-axis) as a function of the BET surface area of the TiO_2 support (BET TiO_2) for a nominal iridium oxide film thickness of $TiO_2 \approx 2$ nm (red line) and t $TiO_2 \approx 4$ nm (purple line). Reproduce with permission [161]. Copyright 2019, The Author(s). (g) Contact resistance of one flow-field/PTL interface for carbon paper and titanium PTLs *vs.* compressive force on the PTL. Reproduce with permission [159]. Copyright 2021, The Author(s). (h) A schematic diagram of an ordered MEA with gradient tapered arrays with its performance. Reproduce with permission [166]. Copyright 2022, American Chemical Society.

lower than the counterpart of the benchmark (~100 m^2/g). However, the thickness ratio of P2X and the benchmark was estimated as ~2 nm/6 nm = 1/3. Apart from the relatively high intrinsic activity of P2X due to its surface amorphous IrO_2 layer, the successive conductive layer was constructed due to its relatively high pack density. The authors also elucidated the relationship between contact resistance at the anode/PTLs and the conductivity of IrO_2 catalysts [159]. Notably, low Ir-loading catalysts enabled to fulfill the target of TiO_2 in Fig. 10f), and thus obtain a successive conductivity layer and reduce Ir loadings. With the decrease of TiO_2 support in specific surface area, however, the intrinsic conductivity of TiO_2 also dominated the catalysts, severely suppressing the electron transfer. Besides, contact resistance can be affected by applied compressive force (Fig. 10g). The increasing compressive force led to a decrease in contact resistance. Nevertheless, it induced the destruction of the proton exchange membrane and carbon PTLs at cathode. In the meanwhile, the compact structures in MEA impart some difficulties in mass transfer, which further causes the voltage loss, especially at high current density.

Mass transfer is also one of the key factors in kinetics losses, which will impart the water adsorption and gas bubbles desorption. PTLs are known for transporting gas from catalyst layers and supporting catalyst layers, which need a large pore for water transfer and a big contact area for low contact resistance. Thus, its porosity, contact area, thickness, and electrical performance are vital to the electrochemical performance of PEMWE. Besides, a porous catalyst layer is favorable to fast mass transfer, whereas it will require a high Ir mass loading for forming a continuous conductivity network. Ideally, two-dimensional and porous catalysts are promising to meet synthetic improvements in electrical conductivity and mass transfer. Recently, some focus has been on the fabrication of ordered MEA [166,167]. Yang *et al.* [166] designed an ordered MEA with gradient tapered arrays *via* nanoimprinting method (Fig. 10h), which maximized the triple-phase interface for rapid mass transport. In the meanwhile, this nanoimprinting method can effectively utilize the Ir catalysts on the gradient structure with close contact. Therefore, the ordered MEA on PEMWE showed a 4.2 time increase in electrochemical active area and a

13.9% improvement in mass transport, resulting in a superior performance (1.801 V@2 A/cm^2). In summary, catalysts and their related system mainly in conductivity, active site density, and mass transfer are synthetic to promote and promise superior activity and durability for a complex PEMWE.

5. Conclusions and outlooks

Ir is the most widely applied on anode material in PEMWE due to its excellent durability and activity under acid conditions. Until now, the reduction of the Ir loadings on the anode is still a great challenge, among which supported Ir catalysts are the most promising method to trade off its activity, durability and mass loadings. Based on the discussion of its application on PEMWE, apart from Ir-based materials, PTLs and MEA assemble parameters are of vital importance to its electrochemical performance on PEMWE, especially the factor of ohmic resistance. Accordingly, some outlooks are presented to address and accelerate the deployment of PEMWE.

5.1. Elucidating its reaction mechanisms with advanced in situ/operando technologies

Ir-based catalysts have achieved great success in terms of their electrochemical performance. Therefore, AEM and LOM are proposed to elucidate the activity and stability of catalysts. Though LOM can give a relatively reasonable analysis of its activity and stability, persistent lattice oxygen participation induces structural collapses, which makes it difficult to maintain its long lifetime. In addition, the inverse relationships of activity and stability are ambiguous. Furthermore, the factor of conductivity is also included to elucidate its activity and degradation. In view of such a nano-micro-environment, even single atoms, the determinations of active sites, composition evolution and key intermediates, such as *in situ*/operando techniques are still difficult. The detected information can assist to describe and elucidate the intrinsic mechanism. Some *in situ*/operando technologies, such as DEMS coupled with ICP-MS, nap-XPS, *in situ* Raman, can monitor real-time structure evolution under real operation at an atomic level. Therefore, thiese information favors the elucidation of real active sites, key intermediates, and structural evolution, deepening the understanding of the oxygen evolution process.

5.2. Constructing a normalized description of ir-based catalysts

The continuous breakthroughs in activity and durability seem to bring a favorable situation based on the analysis of electrical structures of Ir-based catalysts; however, it is unconvincing to explain its relationships of activity and stability with various parameters, such Ir-O covalency, O 2p bands and its Ir-O-M species. Though, seemingly, these parameters are appropriate to construct a structure-activity relationship, it is difficult to make a normalized description to be applied to all Ir-based catalysts. Therefore, the key parameters can be further explored to describe their effect on the electrochemical performance of Ir-based catalysts.

5.3. The utilization of surface reconstruction to trade off its activity and stability

Indeed, the most stable structure is favorable for practical needs in PEMWE. Nevertheless, it faces such a challenge in inert site density. It is feasible to regulate surface reconstruction for highly efficient and stable water oxidation *via* partial element dissolution. The easily leached element can fasten the surface reconstruction of IrO_x species and manipulate the electrical structures of Ir sites for fast proton-coupled electron transfer, which is in agreement with the inverse relationship of activity and stability. In recent future, more attention should be paid to the trade-off between activity and stability. Based on surface reconstruction, the exploration of the active site evolution under service conditions can shed light on guiding efficient and stable catalysts for water oxidation.

5.4. Developing practical Ir-based catalysts in terms of activity and stability

On a three-electrode system, Ir-based catalysts can show a favorable electrochemical performance. However, weak conductivity and element leaching still pose a great difficulty in PEMWE, especially under high potentials. Therefore, enormous attention is paid to developing innovative Ir-based materials with high activity site density, electrical conductivity, mass transfer kinetics and durability. Furthermore, an appropriate model system needs to be constructed for elucidating the ohmic-resistance-induced potential loss. It urges to optimize the assembly techniques of PEMWE for low ohmic resistance, especially contact resistance between PTLs and catalyst layers, and in-plane conductivity of catalyst layers.

5.5. Designing and performing theoretical studies and prediction

Theoretical studies and prediction enable to elucidation of the electronic states, key intermediate, and reaction routes of catalysts, which breaks the limitation of uncertainty of physical and chemical characterization technologies. In the last decades, computational hydrogen electrode (CHE) method based on density functional theory (DFT) has been widely applied in the electrocatalysis area. Though the CHE method provides special insight into understanding the electronic structure and reaction routes of catalysts, its simplifications, and assumptions ignore dynamic evolution at the interface of catalysts and electrolytes. Hence, the challenge for DFT studies in the electrochemical area is the fine control of the electric field, which reflects the electronic structure and dynamics at the interface for a real reaction. Besides, a real reaction condition, such as solvent molecules, the local pH value, explicit treatment, and so on, should be considered to simulate and present a real electrochemical reaction. In the meanwhile, the simplified models can be further modified *via* high-throughput screening to reach the real structures of catalysts. One anticipates that the interdisciplinary study in theoretical simulation and advanced characterization technologies can promote the fabrication of OER catalysts and a deep understanding of its key intermediate evolution.

Declaration of competing interest

The authors declare that they have no known competing financial interests or personal relationships that could have appeared to influence the work reported in this paper.

CRediT authorship contribution statement

Jiawei Ge: Conceptualization, Data curation, Formal analysis, Investigation, Methodology, Resources, Software, Validation, Visualization, Writing – original draft, Writing – review & editing. **Xian Wang:** Supervision, Validation. **Heyuan Tian:** Methodology. **Hao Wan:** Project administration. **Wei Ma:** Software. **Jiangying Qu:** Project administration, Supervision, Validation. **Junjie Ge:** Conceptualization, Funding acquisition, Project administration, Supervision, Validation.

Acknowledgments

The work was supported by the National Key Research and Development Program of China (No. 2022YFB4004100), National

Natural Science Foundation of China (Nos. U22A20396, 22209168), Natural Science Foundation of Anhui Province (No. 2208085UD04), Liaoning Binhai Laboratory (No. LBLF-2023–04), and Shandong Energy Institute (No. SEI U202307).

References

[1] S. Chu, A. Majumdar, Nature 488 (2012) 294–303.
[2] Z. Liu, Z. Deng, S. Davis, P. Ciais, Nat. Rev. Earth Environ. 4 (2023) 205–206.
[3] Z. Lei, T. Wang, B. Zhao, et al., Adv. Energy Mater. 10 (2020) 2000478.
[4] O.S. Bushuyev, P. De Luna, C.T. Dinh, et al., Joule 2 (2018) 825–832.
[5] P. Moriarty, D. Honnery, Int. J. Hydr. Energy 32 (2007) 1616–1624.
[6] G. Glenk, S. Reichelstein, Nat. Energy 4 (2019) 216–222.
[7] M. Chatenet, B.G. Pollet, D.R. Dekel, et al., Chem. Soc. Rev. 51 (2022) 4583–4762.
[8] R.T. Liu, Z.L. Xu, F.M. Li, et al., Chem. Soc. Rev. 52 (2023) 5652–5683.
[9] L. Chong, G. Gao, J. Wen, et al., Science 380 (2023) 609–616.
[10] A. Weiß, A. Siebel, M. Bernt, et al., J. Electrochem. Soc. 166 (2019) F487–F497.
[11] T. Reier, H.N. Nong, D. Teschner, R. Schlögl, P. Strasser, Adv. Energy Mater. 7 (2017) 1601275.
[12] L.W. Chen, H.W. Liang, Catal. Sci. Technol. 11 (2021) 4673–4689.
[13] L. An, C. Wei, M. Lu, et al., Adv. Mater. 33 (2021) 2006328.
[14] Y. Jiao, Y. Zheng, M. Jaroniec, S.Z. Qiao, Chem. Soc. Rev. 44 (2015) 2060–2086.
[15] N.T. Suen, S.F. Hung, Q. Quan, et al., Chem. Soc. Rev. 46 (2017) 337–365.
[16] K. Zhang, X. Liang, L. Wang, et al., Nano Res. Energy 1 (2022) e9120032.
[17] C. Wang, Q. Zhang, B. Yan, et al., Nano-Micro Lett. 15 (2023) 52.
[18] X. Xie, L. Du, L. Yan, et al., Adv. Funct. Mater. 32 (2022) 2110036.
[19] S. Barwe, J. Masa, C. Andronescu, et al., Angew. Chem. Int. Ed. 56 (2017) 8573–8577.
[20] S.R. Kelly, H.H. Heenen, N. Govindarajan, K. Chan, J.K. Nørskov, J. Phys. Chem. C 126 (2022) 5521–5528.
[21] X. Shao, M. Liang, M.G. Kim, et al., Adv. Funct. Mater. 33 (2023) 2211192.
[22] J. Kwon, S. Sun, S. Choi, et al., Adv. Mater. 35 (2023) 2300091.
[23] G.T.K.K. Gunasooriya, J.K. Nørskov, ACS Energy Lett. 5 (2020) 3778–3787.
[24] J. Yu, Q. He, G. Yang, et al., ACS Catal. 9 (2019) 9973–10011.
[25] Y. Chen, C. Liu, J. Xu, et al., Small Struct. 4 (2023) 2200130.
[26] H. Vogt, R.J. Balzer, Electrochim. Acta 50 (2005) 2073–2079.
[27] L. Lao, C. Ramshaw, H. Yeung, J. Appl. Electrochem. 41 (2011) 645–656.
[28] N. Bidin, S.R. Azni, S. Islam, et al., Int. J. Hydr. Energy 42 (2017) 16325–16332.
[29] J. Zhang, L. Zhang, J. Liu, et al., Nat. Commun. 13 (2022) 5497.
[30] N. Zhang, Y. Chai, Energ. Environ. Sci. 14 (2021) 4647–4671.
[31] N.T.T. Thao, J.U. Jang, A.K. Nayak, H. Han, Small Sci. 135 (2023) 2300109.
[32] B.S. Lee, S.H. Ahn, H.Y. Park, et al., Appl. Catal. B 179 (2015) 285–291.
[33] Z. Shi, Y. Wang, J. Li, et al., Joule 5 (2021) 2164–2176.
[34] Q. Wang, X. Huang, Z.L. Zhao, et al., J. Am. Chem. Soc. 142 (2020) 7425–7433.
[35] J. Yin, J. Jin, M. Lu, et al., J. Am. Chem. Soc. 142 (2020) 18378–18386.
[36] L. Yang, G. Yu, X. Ai, et al., Nat. Commun. 9 (2018) 5236.
[37] P.E. Pearce, A.J. Perez, G. Rousse, et al., Nat. Mater. 16 (2017) 580–586.
[38] G. Wu, X. Zheng, P. Cui, et al., Nat. Commun. 10 (2019) 4855.
[39] D. Wu, K. Kusada, S. Yoshioka, et al., Nat. Commun. 12 (2021) 1145.
[40] S. Lee, Y.J. Lee, G. Lee, A. Soon, Nat. Commun. 13 (2022) 3171.
[41] J. Cao, T. Mou, B. Mei, et al., Angew. Chem. Int. Ed. 62 (2023) e202310973.
[42] A.R. Akbashev, V. Roddatis, C. Baeumer, et al., Energ. Environ. Sci. 16 (2023) 513–522.
[43] F.Y. Chen, Z.Y. Wu, Z. Adler, H. Wang, Joule 5 (2021) 1704–1731.
[44] Z. Chen, X. Duan, W. Wei, S. Wang, B.J. Ni, Nano Energy 78 (2020) 105270.
[45] J. Li, Nano-micro Lett. 14 (2022) 112.
[46] C. Wang, L. Jin, H. Shang, et al., Chin. Chem. Lett. 32 (2021) 2108–2116.
[47] L. Yang, L. Shi, H. Chen, et al., Adv. Mater. 35 (2023) 2208539.
[48] I.C. Man, H.Y. Su, F.C. Vallejo, et al., ChemCatChem 3 (2011) 1159–1165.
[49] J.H. Montoya, L.C. Seitz, P. Chakthranont, et al., Nat. Mater. 16 (2017) 70–81.
[50] T. Wu, X. Ren, Y. Sun, et al., Nat. Commun. 12 (2021) 3634.
[51] S. Chen, S. Zhang, L. Guo, et al., Nat. Commun. 14 (2023) 4127.
[52] J. Shan, T. Ling, K. Davey, Y. Zheng, S.Z. Qiao, Adv. Mater. 31 (2019) e1900510.
[53] Q. Xu, J. Zhang, H. Zhang, et al., Energy Environ. Sci. 14 (2021) 5228–5259.
[54] Z. Zhang, P. Ma, L. Luo, et al., Angew. Chem. Int. Ed. 62 (2023) e202216837.
[55] X. Rong, J. Parolin, A.M. Kolpak, ACS Catal. 6 (2016) 1153–1158.
[56] S. Czioska, A. Boubnov, D. Escalera-López, et al., ACS Catal. 11 (2021) 10043–10057.
[57] R.V. Mom, L.J. Falling, O. Kasian, et al., ACS Catal. 12 (2022) 5174–5184.
[58] R. Zhang, N. Dubouis, M. BenOsman, et al., Angew. Chem. Int. Ed. 58 (2019) 4571–4575.
[59] H. Wang, T. Zhai, Y. Wu, et al., Adv. Sci. 10 (2023) 2301706.
[60] D. Zhong, T. Li, D. Wang, et al., Nano Res. 15 (2022) 162–169.
[61] Y. Sun, H. Liao, J. Wang, et al., Nat. Catal. 3 (2020) 554–563.
[62] J. Wu, W. Zou, J. Zhang, et al., Small 20 (2024) 2308419.
[63] K. Zhu, F. Shi, X. Zhu, W. Yang, Nano Energy 73 (2020) 104761.
[64] A. Wang, W. Wang, J. Xu, et al., Mater. Chem. Front. 7 (2023) 5187–5214.
[65] J. Liang, X. Gao, K. Xu, et al., Small 19 (2023) 2304889.
[66] J. Wang, Chem 9 (2023) 1645–1657.
[67] C. Lin, J.L. Li, X. Li, et al., Nat. Catal. 4 (2021) 1012–1023.
[68] S. Bo, F. Tang, H. Su, et al., Catal. Sci. Technol. 12 (2022) 6875–6882.
[69] J.W. Zhao, H. Zhang, C.F. Li, et al., Energy Environ. Sci. 15 (2022) 3912–3922.
[70] R. Mondal, N.K. Mishra, M. Singh, A. Gupta, P. Singh, Phys. Chem. Chem. Phys. 24 (2022) 28584–28598.
[71] W. Wang, Z. Wang, Y. Hu, Y. Liu, S. Chen, eScience 2 (2022) 438–444.
[72] H.N. Nong, L.J. Falling, A. Bergmann, et al., Nature 587 (2020) 408–413.
[73] A. Lončar, D.E. López, S. Cherevko, N. Hodnik, Angew. Chem. Int. Ed. 61 (2022) e202114437.
[74] A. Zagalskaya, V. Alexandrov, ACS Catal. 10 (2020) 3650–3657.
[75] R. Zhang, P.E. Pearce, Y. Duan, et al., Chem. Mater. 31 (2019) 8248–8259.
[76] S. Geiger, O. Kasian, M. Ledendecker, et al., Nat. Catal. 1 (2018) 508–515.
[77] O. Kasian, J.P. Grote, S. Geiger, S. Cherevko, K.J.J. Mayrhofer, Angew. Chem. Int. Ed. 57 (2018) 2488–2491.
[78] H. Over, ACS Catal. 11 (2021) 8848–8871.
[79] S. Choi, J. Park, M.K. Kabiraz, et al., Adv. Funct. Mater. 30 (2020) 2003935.
[80] S. Cherevko, S. Geiger, O. Kasian, A. Mingers, K.J. Mayrhofer, J. Electroanal. Chem. 773 (2016) 69–78.
[81] S. Cherevko, A.R. Zeradjanin, A.A. Topalov, et al., ChemCatChem 6 (2014) 2219–2223.
[82] G.C. da Silva, S.I. Venturini, S. Zhang, et al., ChemElectroChem 7 (2020) 2330–2339.
[83] M. Ledendecker, S. Geiger, K. Hengge, et al., Nano Res. 12 (2019) 2275–2280.
[84] J. Knoppel, M. Mockl, D. Escalera-Lopez, et al., Nat. Commun. 12 (2021) 2231.
[85] W. Huo, X. Zhou, Y. Jin, et al., Small 19 (2023) 2207847.
[86] J. Gao, C.Q. Xu, S.F. Hung, et al., J. Am. Chem. Soc. 141 (2019) 3014–3023.
[87] P. Jovanovič, N. Hodnik, F. Ruiz-Zepeda, et al., J. Am. Chem. Soc. 139 (2017) 12837–12846.
[88] M. Scohy, S. Abbou, V. Martin, et al., ACS Catal. 9 (2019) 9859–9869.
[89] C. Guo, Y. Zheng, J. Ran, et al., Angew. Chem. Int. Ed. 56 (2017) 8539–8543.
[90] J. Li, Y. Zhu, W. Chen, et al., Joule 3 (2019) 557–569.
[91] H.B. Tao, Y. Xu, X. Huang, et al., Joule 3 (2019) 1498–1509.
[92] S. Fleischmann, Y. Zhang, X. Wang, et al., Nat. Energy 7 (2022) 222–228.
[93] P.E. Pearce, C. Yang, A. Iadecola, et al., Chem. Mater. 31 (2019) 5845–5855.
[94] A.J. Perez, R. Beer, Z. Lin, et al., Adv. Energy Mater. 8 (2018) 1702855.
[95] Z. Wang, Y.R. Zheng, I. Chorkendorff, J.K. Nørskov, ACS Energy Lett. 5 (2020) 2905–2908.
[96] H.S. Oh, H.N. Nong, T. Reier, M. Gliech, P. Strasser, Chem. Sci. 6 (2015) 3321–3328.
[97] M. Bernt, A. Siebel, H.A. Gasteiger, J. Electrochem. Soc. 165 (2018) F305–F314.
[98] E. Willinger, C. Massué, R. Schlögl, M.G. Willinger, J. Am. Chem. Soc. 139 (2017) 12093–12101.
[99] D. Cao, Z. Zhang, Y. Cui, et al., Angew. Chem. Int. Ed. 62 (2023) e202214259.
[100] K. Jiang, M. Luo, M. Peng, et al., Nat. Commun. 11 (2020) 2701.
[101] Y.T. Kim, P.P. Lopes, S.A. Park, et al., Nat. Commun. 8 (2017) 1449.
[102] H. Yu, N. Danilovic, Y. Wang, et al., Appl. Catal. B: Environ. 239 (2018) 133–146.
[103] N. Danilovic, R. Subbaraman, K.C. Chang, et al., Angew. Chem. Int. Ed. 53 (2014) 14016–14021.
[104] S. Li, C. Xi, Y.Z. Jin, et al., ACS Energy Lett. 4 (2019) 1823–1829.
[105] E.J. Kim, J. Shin, J. Bak, et al., Appl. Catal. B: Environ. 280 (2021) 119433.
[106] C. Lee, K. Shin, Y. Park, et al., Adv. Funct. Mater. 33 (2023) 2301557.
[107] L. Gu, J. Qi, H. Zeng, et al., ACS Appl. Energy Mater. 6 (2023) 1439–1448.
[108] S. Ganguly, R. Datta, P. Basera, et al., ACS Sustain. Chem. Eng. 12 (2024) 849–859.
[109] Y. Sun, R. Li, X. Chen, et al., Adv. Energy Mater. 11 (2021) 2003755.
[110] A. Zagalskaya, V. Alexandrov, J. Phys. Chem. Lett. 11 (2020) 2695–2700.
[111] Q. Dang, H. Lin, Z. Fan, et al., Nat. Commun. 12 (2021) 6007.
[112] N. Diklić, A.H. Clark, J. Herranz, et al., ACS Catal. 13 (2023) 11069–11079.
[113] Y. He, F. Yan, X. Zhang, et al., Adv. Energy Mater. 13 (2023) 2204177.
[114] M. Elmaalouf, M. Odziomek, S. Duran, et al., Nat. Commun. 12 (2021) 3935.
[115] M. Li, M. Song, W. Ni, et al., Chin. Chem. Lett. 34 (2023) 107571.
[116] L. Fu, X. Zeng, C. Huang, et al., Inorg. Chem. Front. 5 (2018) 1121–1125.
[117] E. Achilli, S. Minelli, I. Casale, et al., Electrochim. Acta 444 (2023) 142017.
[118] R.E. Warburton, P. Hutchison, M.N. Jackson, et al., J. Am. Chem. Soc. 142 (2020) 20855–20864.
[119] Y. Wen, C. Liu, R. Huang, et al., Nat. Commun. 13 (2022) 4871.
[120] W. Zhao, F. Xu, L. Liu, M. Liu, B. Weng, Adv. Mater. 35 (2023) 2308060.
[121] M. Kim, J. Park, M. Wang, et al., Appl. Catal. B: Environ. 302 (2022) 120834.
[122] Y. Zhu, J. Wang, T. Koketsu, et al., Nat. Commun. 13 (2022) 7754.
[123] Z. Zhang, C. Feng, D. Wang, et al., Nat. Commun. 13 (2022) 2473.
[124] L.Y. Chueh, C.H. Kuo, R.H. Yang, et al., Chem. Eng. J 464 (2023) 142613.
[125] L. Li, P. Wang, Z. Cheng, Q. Shao, X. Huang, Nano Res. 15 (2021) 1087–1093.
[126] F. Luo, L. Guo, Y. Xie, et al., Appl. Catal. B: Environ. 279 (2020) 119394.
[127] L. Yang, K. Zhang, H. Chen, et al., J. Energy Chem. 66 (2022) 619–627.
[128] D. Böhm, M. Beetz, M. Schuster, et al., Adv. Funct. Mater. 30 (2020) 1906670.
[129] L. Zhuang, F. Xu, K. Wang, et al., Small 17 (2021) 2100121.
[130] J.A. Hoffman, Z.S.H.S. Rajan, D. Susac, M.C. Matoetoe, R. Mohamed, J. Phys. Chem. C 127 (2023) 894–906.
[131] B. Huang, Y. Zhao, EcoMat 4 (2022) e12176.
[132] F. Liao, K. Yin, Y. Ji, et al., Nat. Commun. 14 (2023) 1248.
[133] B. Jiang, Y. Guo, J. Kim, et al., J. Am. Chem. Soc. 140 (2018) 12434–12441.
[134] G. Jiang, H. Yu, J. Hao, et al., J. Energy Chem. 39 (2019) 23–28.
[135] S. Zhang, L. Yin, Q. Li, et al., Chem. Sci. 14 (2023) 5887–5893.
[136] N. Zhang, J. Du, N. Zhou, et al., Chin. J. Catal. 53 (2023) 134–142.
[137] H. Wu, Y. Wang, Z. Shi, et al., J. Phys. Chem. C 127 (2023) 12541–12547.
[138] J. Shan, C. Ye, S. Chen, et al., J. Am. Chem. Soc 143 (2021) 5201–5211.
[139] S. Kumari, B.P. Ajayi, B. Kumar, et al., Energ. Environ. Sci. 10 (2017) 2432–2440.
[140] W. Sun, Y. Song, X.Q. Gong, L.m. Cao, J. Yang, Chem. Sci. 6 (2015) 4993–4999.
[141] Y. Wang, R. Ma, Z. Shi, et al., Chem 9 (2023) 2931–2942.

[142] W. Zhu, X. Song, F. Liao, et al., Nat. Commun. 14 (2023) 5365.
[143] F.F. Zhang, C.Q. Cheng, J.Q. Wang, et al., ACS Energy Lett. 6 (2021) 1588–1595.
[144] S. Hao, H. Sheng, M. Liu, et al., Nat. Nanotechnol. 16 (2021) 1371–1377.
[145] L. Jin, H. Pang, Chin. Chem. Lett. 31 (2020) 2300–2304.
[146] P. Han, T. Tan, F. Wu, et al., Chin. Chem. Lett. 31 (2020) 2469–2472.
[147] C. Yang, X. Zhang, Q. An, et al., J. Energy Chem. 78 (2023) 374–380.
[148] X. Zheng, J. Yang, P. Li, et al., Sci. Adv. 9 (2023) eadi8025.
[149] H. Su, W. Zhou, W. Zhou, et al., Nat. Commun. 12 (2021) 6118.
[150] Z. Shi, J. Li, J. Jiang, et al., Angew. Chem. Int. Ed. 61 (2022) e202212341.
[151] X. Liu, S. Xi, H. Kim, et al., Nat. Commun. 12 (2021) 5676.
[152] H.J. Song, H. Yoon, B. Ju, D.W. Kim, Adv. Energy Mater. 11 (2020) 2002428.
[153] H. Wang, J. Wang, Y. Pi, et al., Angew. Chem. Int. Ed. 131 (2019) 2338–2342.
[154] D.F. Abbott, R.K. Pittkowski, K. Macounova, et al., ACS Appl. Mater. 11 (2019) 37748–37760.
[155] M. Retuerto, L. Pascual, J. Torrero, et al., Nat. Commun. 13 (2022) 7935.
[156] Q. Zhang, X. Liang, H. Chen, et al., Chem. Mater. 32 (2020) 3904–3910.
[157] C. Shang, C. Cao, D. Yu, et al., Adv. Mater. 31 (2018) 1805104.
[158] J. Torrero, T. Morawietz, D.García Sanchez, et al., Adv. Energy Mater. 13 (2023) 2204169.
[159] M. Bernt, C. Schramm, J. Schröter, et al., J. Electrochem. Soc. 168 (2021) 084513.
[160] M. Bernt, J. Schröter, M. Möckl, H.A. Gasteiger, J. Electrochem. Soc. 167 (2020) 124502.
[161] C. Simon, J. Endres, B.N. Loders, F. Wilhelm, H.A. Gasteiger, J. Electrochem. Soc. 166 (2019) F1022–F1035.
[162] M. Bernt, H.A. Gasteiger, J. Electrochem. Soc. 163 (2016) F3179–F3189.
[163] T.B.N. Huynh, J. Song, H.E. Bae, et al., Adv. Funct. Mater. 33 (2023) 2301999.
[164] J. Lim, G. Kang, J.W. Lee, et al., J. Power Sources 524 (2022) 231069.
[165] M. Möckl, M.F. Ernst, M. Kornherr, et al., J. Electrochem. Soc. 169 (2022) 064505.
[166] S. Dong, C. Zhang, Z. Yue, et al., Nano Lett. 22 (2022) 9434–9440.
[167] B. Tian, Y. Li, Y. Liu, et al., Nano Lett. 23 (2023) 6474–6481.